Research Article

Hydrodynamics and sedimentary processes in the modern Rion strait (Greece): Interplay between tidal currents and internal tides

Romain Rubi [a,*], Aurélia Hubert-Ferrari [a], Elias Fakiris [b], Dimitris Christodoulou [b], Xenophon Dimas [b], Maria Geraga [b], George Papatheodorou [b], Basile Caterina [a]

[a] *Dept. of Physical Geography and Quaternary, University of Liège, Liège, Belgium*
[b] *Laboratory of Marine Geology and Physical Oceanography, Geology Department, University of Patras, Greece*

ABSTRACT

Straits are crossed by marine currents that are amplified due to constrictions. These nearshore high-velocity flows are problematic for offshore infrastructures (bridge pillars, cables, pipelines, etc), but constitute an interesting carbon-free energy source. Many modern straits are dominated by tidal currents which flow axially, with reversal directions and phase difference between the two interlinked basins. These tidal currents interplay with: sediment sources (including in situ carbonate production and deltas), tectonic activity, and inherited lowstand features, all shaping the seafloor into complex geomorphologies. Previous studies have highlighted a common tidal strait depositional model with a strait-center zone in erosion and on each side a dune-bedded strait zone with 3D and 2D tidal dunes and tidal ripples. Even if the internal waves associated with and generated by the straits are widely documented, the effects of the internal waves on the seafloor need to be further investigated. The aim of this study is to unravel the combined effects of the tidal currents and the internal tides on current pattern and on the morphosedimentary features.

We present a strait example based on an interdisciplinary approach using high-resolution geophysical and oceanographical data to better constrain the hydrodynamics and the processes acting on the seafloor. We focus on the Rion Strait in Greece which controls the connection between the Corinth Gulf and the Mediterranean Sea. Based on high-resolution multibeam bathymetry (MBES) over an area of 211 km², we identify and quantify different morphologies by extracting bathymetric swath profiles. These results are integrated with currents data (ADCP) and CTD profiles. In addition, we use high-resolution chirp sub-bottom profiles and sparker seismic reflection profiles to document the morphology and internal architectures of the sedimentary deposits and the erosional features in the strait bottom. To complete this dataset, we analyzed Sea Surface Temperatures (SST) from satellite sensors.

The Rion Strait displays complex bathymetric features without tidal dunes. At the excepted depositional location of tidal dunes, we identify an erosive area with a pool and crest morphology. This new example completes the tidal strait depositional model by a re-localization of erosion, bypass and deposition in an asymmetric strait swept by baroclinic currents. This example illustrates the key role of internal tides in straits located between a confined deep basin and an open sea.

1. Introduction

Sedimentary basins may experience episodic oceanic connections via a strait during their evolution: during their opening and consequent "marine" flooding or during their closure when the connection with the ocean is lost. These straits can be located along overall complex tectonic settings, i.e. at the frontiers of tectonic plates like the Strait of Gibraltar located between the Eurasian and the African plates (Stow et al., 2013) or the Messina Strait between Calabria and Sicily (Bignami et al., 1990; Androsov et al., 1993; Brandt et al., 1997; Ferranti et al., 2008; Longhitano, 2013; Longhitano et al., 2014; Longhitano, 2018a, 2018b). These water passages can be sills which are highly sensitive to climate,

---

sea-level variations and tectonics. Indeed, sills drastically control the paleo-environment like in the Dover Strait which leads to the origin of the Britain Island (Gupta et al., 2017 and references within) or the Gibraltar strait whose closure led to the Messinian Salinity crisis (e.g., Krijgsman et al., 2018; Krijgsman et al., 1999). Theses connections by gateways, straits and seaways are fundamental in terms of water, heat, sediment and biotas transfers from one basin to another and may affect their paleoecology, sedimentology and stratigraphy (Longhitano and Chiarella, 2020). However, these key areas are difficult to study due to their ephemeral nature and so often disregarded in basin evolution.

Present-day straits are usually constricted areas that are known to amplify tides (Defant, 1961; Pugh, 1987). Tidal currents converge axially with reversal directions and phase difference between the two interlinked basins (Pratt and Lundberg, 1991), which generates asymmetric tides (e.g., Reynaud et al., 2013). The associated current velocities may exceed 2 m/s in the narrowest parts, whereas they tend to decelerate towards the strait ends (Malikides et al., 1988; Lindstrom et al., 1990; Santoro et al., 2002). These currents constitute an interesting carbon-free energy source (see e.g. Evans et al., 2015). The depositional model for tidal straits proposed by Longhitano (2013) defines four zones: A) a strait-center zone in erosion with scour and exposed bedrock; B) a dune-bedded strait zone with 3D and 2D tidal dunes; C) a strait-end zone with tidal ripples; and D) a strait-margin zone where deltaic and other nearshore processes interplay with tidal currents.

In addition to tidal currents, internal waves and internal tides are documented in the strait dynamics: in the Luzon Strait (Tian et al., 2006; Yuan et al., 2006; Chao et al., 2007; Jan et al., 2008; Buijsman et al., 2010; Warn-Varnas et al., 2010; Alford et al., 2011; Farmer et al., 2011; Liao et al., 2012; Pinkel et al., 2012; Rainville et al., 2013; Rudnick et al., 2013; Huang et al., 2014); in the Strait of Gibraltar at the Camarinal Sill (Ziegenbein, 1969; Boyce, 1975; Watson and Robinson, 1990; Pistek and La Violette, 1999; Morozov et al., 2002; Vázquez et al., 2008); in the Kara Gates Strait (Morozov et al., 2008, 2017) and in the Messina Strait (Griffa et al., 1986; Sapia and Salusti, 1987; Alpers et al., 1996; Brandt et al., 1997; Droghei et al., 2016). The triggering of internal waves generally occurs on the steep slopes of the straits (Hibiya, 1990; Morozov et al., 2003). Internal waves are observed at the interface between an upper low-density water layer and a bottom higher-density one (Holloway, 1987). An internal wave can evolve into internal hydraulic jumps near a shelf break (Holloway, 1987) or over a steep ridge (Legg and Klymak, 2008). When internal waves are modulated by tidal cyclical changes between the two interconnected basins, they are called internal tides. Even if the internal waves associated and generated by straits are more and more documented, their effects on sediments need to be investigated. There is a gap between the identification of an internal wave, mostly carried out from remote and satellite images, and its effects on the water circulation and the seafloor.

This study focuses on a particular strait and its associated sills: the modern Rion Strait. It is located between a shallow basin, the Patras Gulf, and a deep narrow basin, the Corinth Gulf in Greece (Fig. 1). In the microtidal Mediterranean Sea, the Rion strait hosts reverse tidal currents up to 2 m/s as modelled by Fourniotis and Horsch (2015). Moreover, the two gulfs show a phase difference in tides able to generate horizontal water masses exchanges through the Rion strait (Hadjitheodorou et al., 1992; Fourniotis and Horsch, 2010). The Rion strait connects two different stratified water bodies with contrasted densities between the warmer Ionian waters (28.6–38.7 psu) and the colder Corinth waters (38.3–38.5 psu). These conditions are ideal for the generation of internal waves at the interface between the water bodies. Here, the objective is to unravel the combined effects of the tidal currents and the internal tides on current pattern and their effects on the sea bottom. Published oceanographic data from the Patras and Corinth Gulf are limited, so that the understanding of water circulation is currently rather incomplete. This analysis is based on satellite images and on an oceanographic survey (May 2019) at the sill location which combined: chirp

Sub-Bottom Profiler (SBP), sparker high-resolution seismic reflection survey, multibeam echosounders (MBES), acoustic doppler current profiler (ADCP), Conductivity Temperature and Depth sensor (CTD), and towed underwater camera (Fig. 2).
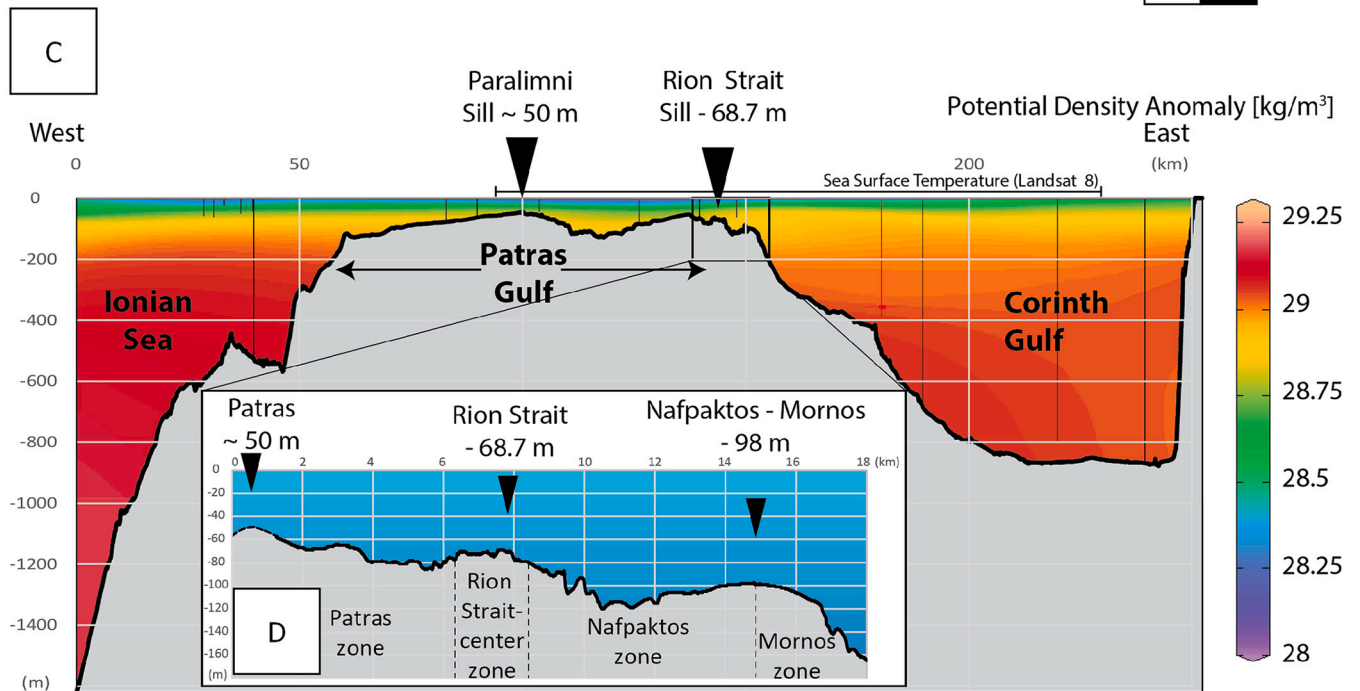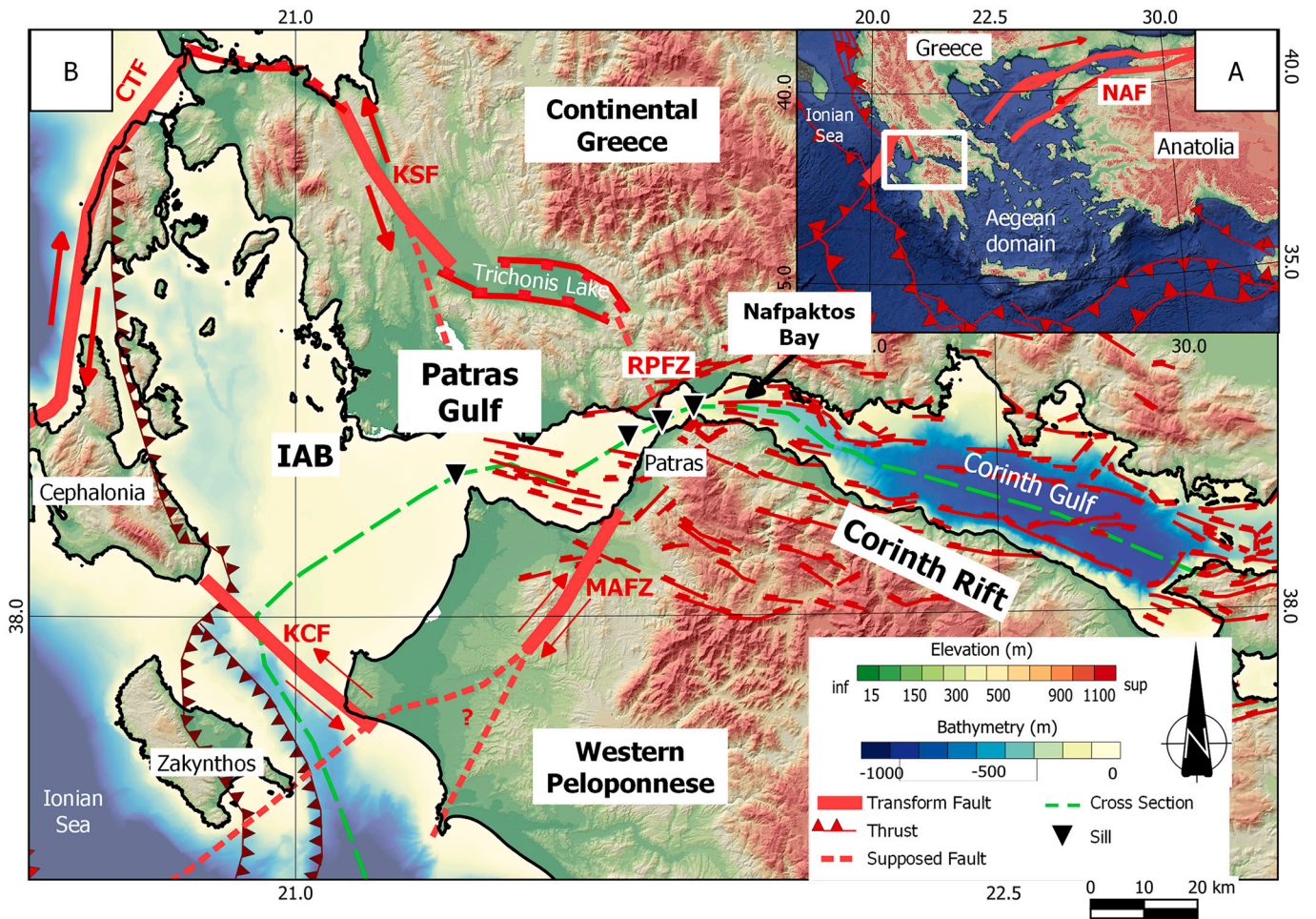
2. Setting

2.1. Regional tectonic setting

The Rion Strait is located at the boundary between two geological basins, the Patras basin or the Ionian Akarnania Block (IAB) to the West and the Corinth rift to the East. Basin deformation takes place within the broader East Mediterranean geodynamic setting governed by the convergence between Africa and Eurasia since the Mesozoic (Menant et al., 2016; Fig. 1A).

The Patras Basin is characterized by strike-slip faulting along its margins (Ferentinos et al., 1985; Hatzfeld et al., 1995; Haslinger, 1998; Sachpazi et al., 2000; Kassaras et al., 2014; Papadopoulos et al., 2014; Pérouse et al., 2017; Haddad et al., 2020). This basin is mostly aseismic and it is bounded to the south-west by the left-lateral Kyllini Cephalonia Fault (KCF), to the north-west by the right-lateral Cephalonia Transform Fault (CTF) and to the north by the left-lateral Katouna-Stamna Fault (KSF, Fig. 1B). According to the geomorphological mapping of Pérouse et al. (2017), the KCF extends from the Amvrakikos Gulf to the Patras Gulf and is associated with extensional deformation around the Trichonis Lake (Fig. 1B). The central and deeper part of the Patras Gulf (138 m) is affected by normal faults (Ferentinos et al., 1985; Fig. 1B). The southern margin of the Patras Basin is weakly constrained by the the Movri Amaliada Fault Zone (MAFZ) which extends to the Rion-Patras Fault Zone (RPFZ, Fig. 1). An offshore drilling in the southern part of the Patras Gulf reveals about 1800 m of Neogene and Plio-Quaternary sediments overlying Triassic anhydrites (Ferentinos et al., 1985). However, the initial opening of the Patra basin and its sedimentary infill remain mainly unknown. The southern shore of the Patras Gulf is flanked by Plio-Quaternary deposits of shallow marine and lagoonal facies which reach a maximum thickness of 1500 m (Hageman, 1979).

To the East, the Corinth rift has been characterized by an extensional area between the continental Greece and the Peloponnese since around c.a. 5 Ma (sensu Papanikolaou and Royden, 2007) and by the uplift of the Peloponnese since 1 Ma. The Corinth rift is bordered by normal faults (Jackson et al., 1982; Armijo et al., 1996; Sakellariou et al., 2001; Moretti et al., 2003) except at its western tip (around the Rion Strait and the Nafpaktos Bay) which is characterized by strike-slip and normal faults (Beckers et al., 2015). Since the upper Pleistocene, the rift basin has alternated between marine conditions during interglacial/highstand periods and endorheic conditions during glacial/lowstand periods, as eustatic sea level fluctuated relative to the boundaries of the basin (Sachpazi et al., 2003; Moretti et al., 2004; Lykousis et al., 2007; Bell et al., 2008; Taylor et al., 2011; Nixon et al., 2016; McNeill et al., 2019). Since at least 200 kyr, the sills at the western mouth of the Corinth Gulf controlled the connection with the Ionian Sea (Fig. 1; Perissoratis et al., 2000; Ford et al., 2013; Beckers et al., 2016). Moreover, the Nafpaktos Bay at the westernmost tip of the Corinth rift presents the highest extensional rate, up to 15–16 mm yr-1, and most of present-day seismicity is concentrated offshore (Briole et al., 2000; Avallone et al., 2004; Bell et al., 2011; Beckers et al., 2015) with more than 30 earthquakes from 2016 to 2017, occurring between 5 and 35 km of depth (Haddad et al., 2020).

2.2. Physiographic and oceanographic settings

The Patras Gulf form a shallow depression with four sills between the open Ionian Sea to the West and the Corinth Gulf to the East (Fig. 1). The Patras Gulf is ~80 km long, up to 20 km wide East of the Paralimni sill and up to 40 km wide West of it, with a mean depth of ~56 m. It reaches the depth of ~138 m in its center (Ferentinos et al., 1985; Fig. 1). The

(caption on next page)

Fig. 1. Settings and location A. Regional East Mediterranean geodynamic context with the North Anatolian Fault (NAF) and the Hellenic trench. B. Topographic, bathymetric and fault map of the Patras and Corinth basins. The aseismic Ionian-Akarnania Block (IAB) is bounded by the Kyllini Cephalonia Fault (KCF), the Cephalonia Transform Fault (CTF), the Katouna-Stamna Fault (KSF), the Rion-Patras Fault Zone (RPFZ) and the Movri Amaliada Fault Zone (MAFZ). C. Bathymetric cross section (dashed green line in inset B) from the Ionian Sea (West) to the Perachora Peninsula (East Corinth Gulf) based on open data from https://portal.emo dnet-bathymetry.eu/. The KCF separates the south-wets of the shallow Patras Gulf from the deep Ionian Sea. The transition between the shallow Patras Gulf and the deep Corinth Gulf is more complex and is located around the Rion Strait and sills and controlled by the Rion-Patras Fault Zone (RPFZ). The Patras Gulf shows the Paralimni sill at ~50 m of depth. The deepest part of the Patras basin is controlled by active normal faults. D. Detailed bathymetric cross section at the transition between the shallow Patras basin and the deep Corinth basin based on this survey bathymetric data. The transition consists of three sills from West to East: the Patras sill (−50 m); the Rion Strait sill (−68.7 m) and the Nafpaktos-Mornos strait sill (−98 m). (For interpretation of the references to colour in this figure legend, the reader is referred to the web version of this article.)
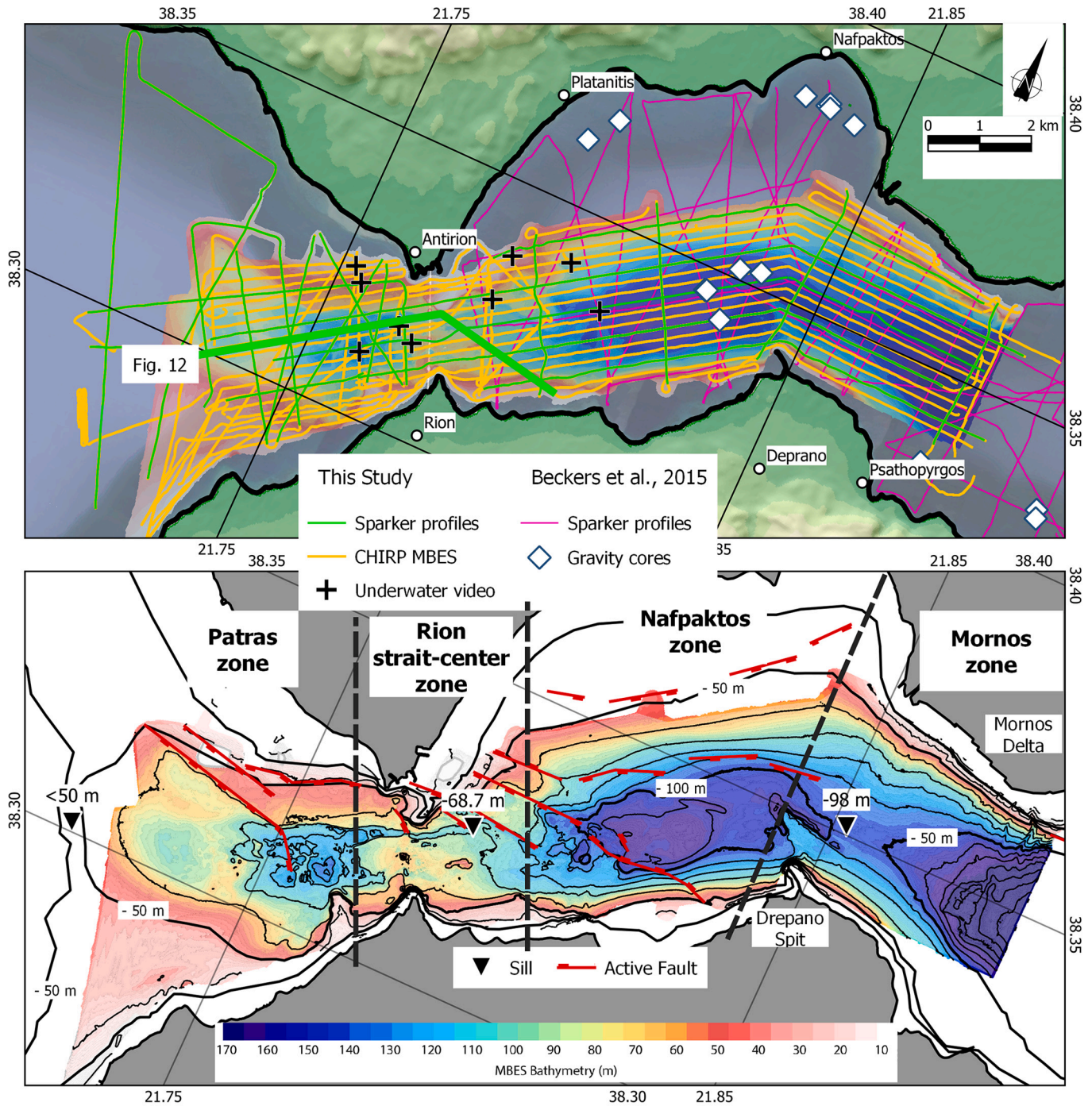

Fig. 2. A. Data map with the location of seismic profiles and underwater videos. B. Detailed multibeam bathymetry (MBES) and strait zones.

westernmost Paralimni sill reaches ~50 m depth and is located between the Acheloos delta and cape Pappas (Fig. 1; Piper et al., 1988). The three other sills are located at the transition between the eastern Patras Gulf and the western Corinth Gulf (Fig. 1). From West to East the sill bathymetries increase with the Patras sill at ~50 m depth, the Rion sill at ~70 m depth and the Nafpaktos-Mornos sill at ~100 m depth (Fig. 1D). The Rion Strait marks the maximum land constriction point at the location of the Rion sill. The Corinth Gulf is a ~ 120 km long, up to ~30 km wide and ~ 800 m deep basin connected at its western tip to the Ionian Sea through the Patras Gulf (Fig. 1). The Corinth Gulf is flanked by steep slopes and high reliefs associated with the rift normal faults (Fig. 1).

Based on salinity distribution, Friligos et al. (1985) documented that the Patras water masses consist of the Ionian water mass (38.6–38.7 psu), the Corinth water mass (38.3–38.5 psu) and some freshwater input (Supp Data Table 5). Thermal stratification occurs during summer but the water body is well mixed during winter in the Patras (Papailiou, 1982) and Corinth basins (Lascaratos et al., 1989; Poulos et al., 1996). In summer, the upper layer shows a strong thermal gradient from 26 °C at the surface to 21 °C at ~60 m depth. Below the thermocline, the temperature is uniformly at 13 °C. In winter, the convection homogenizes the temperature profile around 13 °C (Anderson and Carmack, 1973; Lascaratos et al., 1989; Poulos et al., 1996).

The hydrodynamic circulation understanding is mainly based on remote satellite infrared images (Lascaratos et al., 1989) and the MIKE 3 FM (HD) numerical modelling (Fourniotis and Horsch, 2010, 2015; Horsch and Fourniotis, 2018; Horsch and Fourniotis, 2017). Simulations of Fourniotis and Horsch (2015) show that the circulation is dominated by tides with an average amplitude of 20 cm and a semidiurnal oscillation. The tidal currents are amplified up to 2 m/s through the Rion Strait. Moreover, an internal wave is generated in summer with an amplitude of 20–25 m in this strait (Fourniotis and Horsch, 2015). Northwestern and northeastern winds also play a significant role in the hydrodynamic circulation. The high mountain ranges on both sides funnel these winds that can reach up to 15 m/s. They increase the water exchange flow rate with the Corinth Gulf and cause a deepened thermocline in the Patras Gulf at ~60 m (Fourniotis and Horsch, 2010; Fourniotis and Horsch, 2015; Fourniotis and Horsch, 2015).

Moreover, two upwellings are induced by the baroclinic and barotropic forcing: one on the northern coast of the Nafpaktos bay (Lascaratos et al., 1989) and the other one in front of Patras town (Fourniotis and Horsch, 2015). Two counterclockwise gyres centered in the Corinth and Patras Gulfs are observed at the surface (Lascaratos et al., 1989). In Patras Gulf, this cyclonic gyre is the result of NE winds during flood tide (Fourniotis and Horsch, 2015).

In the deeper Nafpaktos bay, Beckers et al. (2015) document a bottom current system based on seismic profiles. They localized Holocene drifts, up to 45 m thick, on the northern and southern slopes and erosional morphologies in the center of the U-shaped Nafpaktos bay. In the central part of the Corinth Gulf near-bed current meter data suggest that the velocity of the currents is very low (<8 cm/s, Poulos et al., 1996).

3. Data acquisition and methods

To describe the study area, we refer to four zones along the strait zone (Fig. 2). Firstly, the Rion strait-center zone is equivalent to the narrowest axial sector of the strait between the Rion and Antirion towns linked since 2004 by the Charilaos Trikoupis Bridge. Secondly, the Patras zone is located west of the strait and is characterized by an opening to the shallow Patras Gulf and the Patras sill (~50 m, Fig. 1D). Thirdly, the Nafpaktos zone extends east of the strait s.s. until the narrow Nafpaktos-Mornos sill at ~98 m depth (Fig.1D). Fourthly, the Mornos zone is the easternmost part of the study area located east of the Nafpaktos-Mornos sill. This area links the Nafpaktos bay with the Corinth Gulf.

3.1. May 2019 survey

The Rion sill zone was investigated in May 2019 using: a chirp Sub-Bottom Profiler (SBP), a high-resolution seismic reflection sparker, a multibeam echosounder (MBES), an acoustic doppler current profiler (ADCP), a Conductivity Temperature and Depth sensor (CTD), and a towed underwater camera (Fig. 2).

About 420 km of chirp profiles were acquired with a 3.5 kHz sub-bottom profiling system consisting of a Model 5430A GeoPulse Transmitter, a Model 5210A GeoPulse Receiver, a Model 1600 EPC "S" type Graphic Recorder and an O.R.E. Model 132A/132B over-the-side four transducers array (from Papatheodorou et al., 2014). In addition, ~144 km of high-resolution seismic reflection profiles were acquired with a multi-electrode sparker source that produces a broad-spectrum seismic signal, with a mean frequency at ~1.3 kHz. A single channel, high-resolution streamer was used as receiver. A bandpass filter (200–300 to 2000–3000 Hz) was applied to eliminate non-signal noise. The SEG-Y profiles were processed with Seismic Unix (Bleistein et al., 2001). These high-resolution seismic profiles were combined with 2011 and 2012 seismic surveys from R/V ALKYON (Beckers et al., 2015). All the seismic profiles were interpreted in 3D view with GoCAD software (Emerson). MBES and ADCP data were based on the same SBP and sparker profile path.

The MBES characteristics and processing are presented in details in Fakiris et al. (2019) and are summarized briefly below. The MBES data were acquired through Hypack 2016, while Elac's HydroStar software was used as the inertial beam forming navigation and attitude system. A Real Time Kinematics (RTK) GPS was used to obtain a 10 cm lateral positioning accuracy. The MBES survey was performed with a dual-head MBES Elac Nautic Seabeam 1185, transmitting at 180 kHz. Geocoder tool (Hypack 2016 suite software) was used to identify and correct radiometric and geometric MBES backscatter artifacts. The MBES time series were also corrected for the tidal effects based on Patras tidal curves (data from www.worldtides.info). These tidal data are consistent with the CMEMS data (Copernicus Marine Environment Monitoring Service) from the Mediterranean Sea Physics Analysis and Forecast (doi:10.25423/CMCC/MEDSEA_ANALYSISFORECAST_PHY_006_013_EAS6).

The MBES data covered an area of 211 km^2 and provided a 5 m × 5 m lateral resolution bathymetric map. The ADCP and MBES data were calibrated with CTD and sound velocity profiles on the water column using a Valeport MiniSVS-P. The ADCP times series were tied with the Patras tidal curves. The ADCP and CTD data were analyzed with Ocean Data View software (Schlitzer, 2015). The MBES morphologies were displayed with QGIS software and with the extraction of bathymetric swath profiles across curved geomorphic features such as channels (Hergarten et al., 2014).

3.2. SST from CMEMS and Landsat 8

The regional SST data were provided by the CMEMS, based on the L3 multi-sensor (supercollated) product as NetCDF-4 files. The spatial resolution was 0.02 × 0.02 degree and the SST average was calculated on daily mean temperatures from 01 to 01-2019 to 01-01-2020. The raw SST maps are presented on Supp. Fig. 15 as animated gifs for each season based on SST pattern. Furthermore, the entire area was divided in four parts to extract SST values for each region: Ionian, Patras, Nafpaktos, Corinth (see Fig. 3 for area extends). Then, a mean was calculated first along the longitude then along the latitude to get the mean value for each area as a single point.

We used the Landsat 8 images to obtain the Sea Surface Temperature (SST) using its Thermal Infrared Sensor (TIRS) – Band 10 (10.6–11.9 μm) with a resolution of 100 m. We worked on all cloud-free images collected since 2013. Unfortunately, only 30 images from June to November were available.

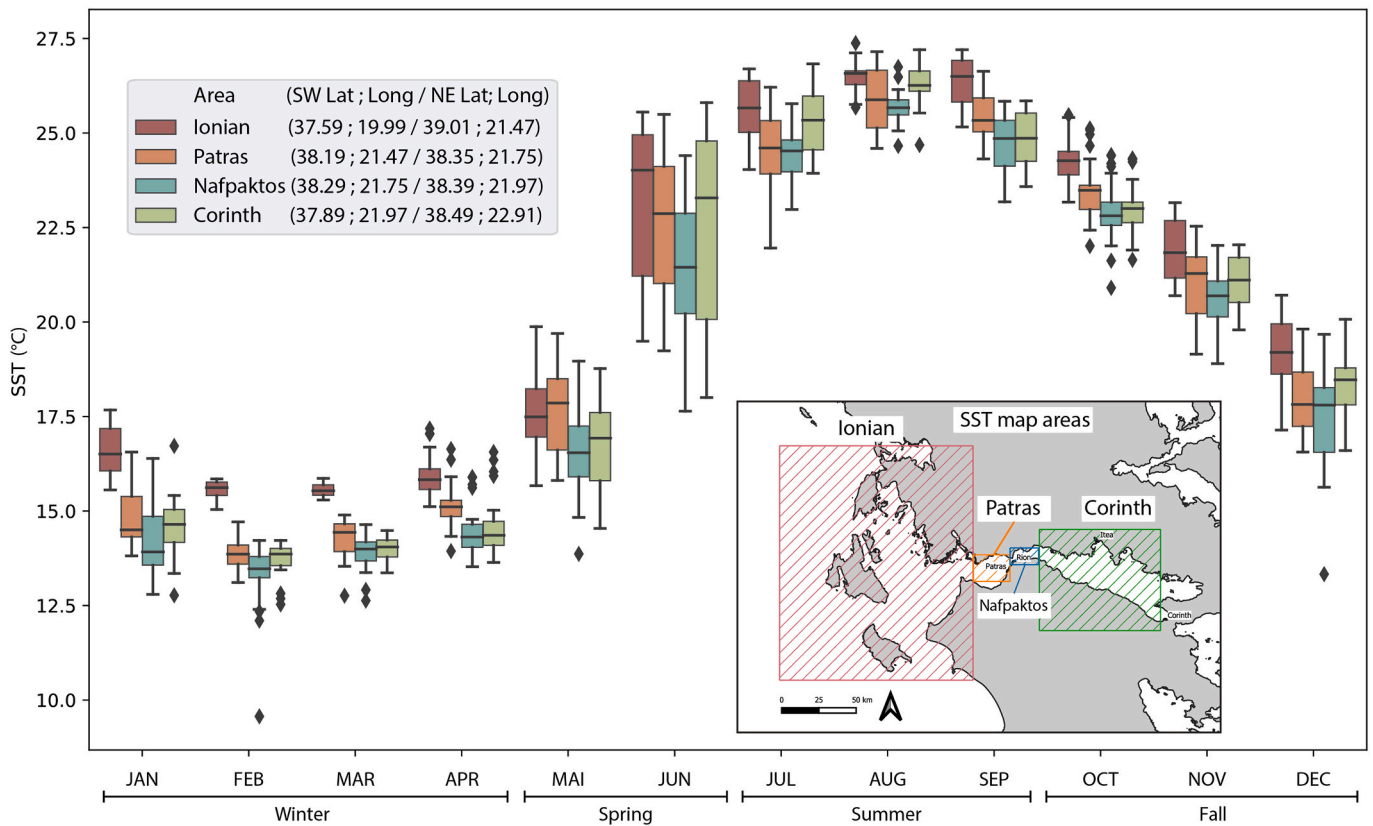We calculate the Top of Atmosphere (TOA) Radiance following eq. 1:

Fig. 3. Monthly Sea Surface Temperature diagram for Ionian; Patras; Nafpaktos; and Corinth areas, data from CMEMS based on daily mean temperatures from 01 to 01-2019 to 01-01-2020. The SST maps are displayed as animated gifts on Supp. Fig. 15 for each season according to the SST trends.

$$L_l = M_L Q_{cal} + A_L \qquad (1)$$

L_l = TOA spectral radiance (Watts/(m2 * srad * μm)).

M_L=Band-specific multiplicative rescaling factor from the metadata (RADIANCE_MULT_BAND_x, where x is the band number).

A_L=Band-specific additive rescaling factor from the metadata (RADIANCE_ADD_BAND_x, where x is the band number).

Q_{cal} = Quantized and calibrated standard product pixel values (DN).

Then, we retrieved the SST by the conversion to the top of atmosphere brightness temperature following eq. 2:

$$T\ (^{\circ}C) = \frac{K_2}{ln\left(\frac{K_1}{L_l} + 1\right)} - 273.15 \qquad (2)$$

T = Top of atmosphere brightness temperature (°C).

K_1 = Band-specific thermal conversion constant from the metadata (K1_CONSTANT_BAND_x, where x is the thermal band number).

K_2 = Band-specific thermal conversion constant from the metadata (K2_CONSTANT_BAND_x, where x is the thermal band number).

4. Results

4.1. Sea surface temperatures (SST)

The SST display a major seasonal variability between the Ionian Sea, Patras and Corinth Gulfs with summer SST up to 26 °C and winter SST below 14 °C (Fig. 3, Supp. Fig. 15). The regional SST show that the open Ionian Sea is hotter than waters of the Corinth and the Patras Gulfs (Figs. 3, Supp. Fig. 15). This had already been observed by Lascaratos et al. (1989), but the regional SST data provide more details. The temperature difference is reduced in summer between the basins (Figs. 3, Supp. Fig. 15), which is not what was observed by Lascaratos et al. (1989) based on NOAA-6 and 7 infrared satellite images from June 1981

to November 1982. The winter time, from January to April is characterized by Ionian waters around 16 °C whereas Patras, Nafpaktos, and Corinth waters have lower temperatures of 14 °C on average. During spring time, from May to June, the temperature rapidly increases and shows a wide range from 15 °C to 25 °C. The summer time, from July to September, presents temperatures between 24° and 26 °C. In August, few inverse SST occur with Corinth waters warmer than Patras ones with differences of 1 °C to 3 °C (for example Fig. 4E). Then, during fall time, the temperatures slowly decrease between October to December. The re-cooling is characterized by SST systematically 2 °C lower in the Corinth Gulf than in the Ionian Sea.

A key observation is that the Nafpaktos Bay and sometimes the Patras Gulf have colder SST than the Corinth Gulf and the Ionian Sea (Figs. 1, 3, 15; Lascaratos et al., 1989). Surprisingly, these lowest SST occurs in the shallowest areas present in the study area, where we would expect to find the warmest temperature. Observations from Landsat 8 thermic images evidence that the SST boundary between the two gulfs is generally localized near the Rion Strait (Fig. 4).

Additionally, Landsat 8 imagery provides more details (2 examples on Fig. 4) and highlights that the cold SST occur mainly in two specific areas between February and May: east of the Mornos Delta (North shore) or west of the Drepano spit (Figs. 2 and 4). The Mornos river discharges have been regulated by a dam since 1979 and this river flows on the western side of the delta while the cold SST are localized on the opposite eastern side, more than 5 km away. To the south, the Volinaios mouth is on the eastern side of Drepano spit. Consequently, it is rather unlikely that the low SST in these areas correspond to the river discharges. In the Patras Gulf, the cold surface water is mainly restricted near the Rion Strait. We interpret these isolated cold SST as the result of an upwelling from the Corinth Gulf to its western shallow tip, i.e. in the Nafpaktos-Mornos areas. This upwelling has been outlined by Lascaratos et al. (1989) which argued for a wind-driven upwelling. Fourniotis and
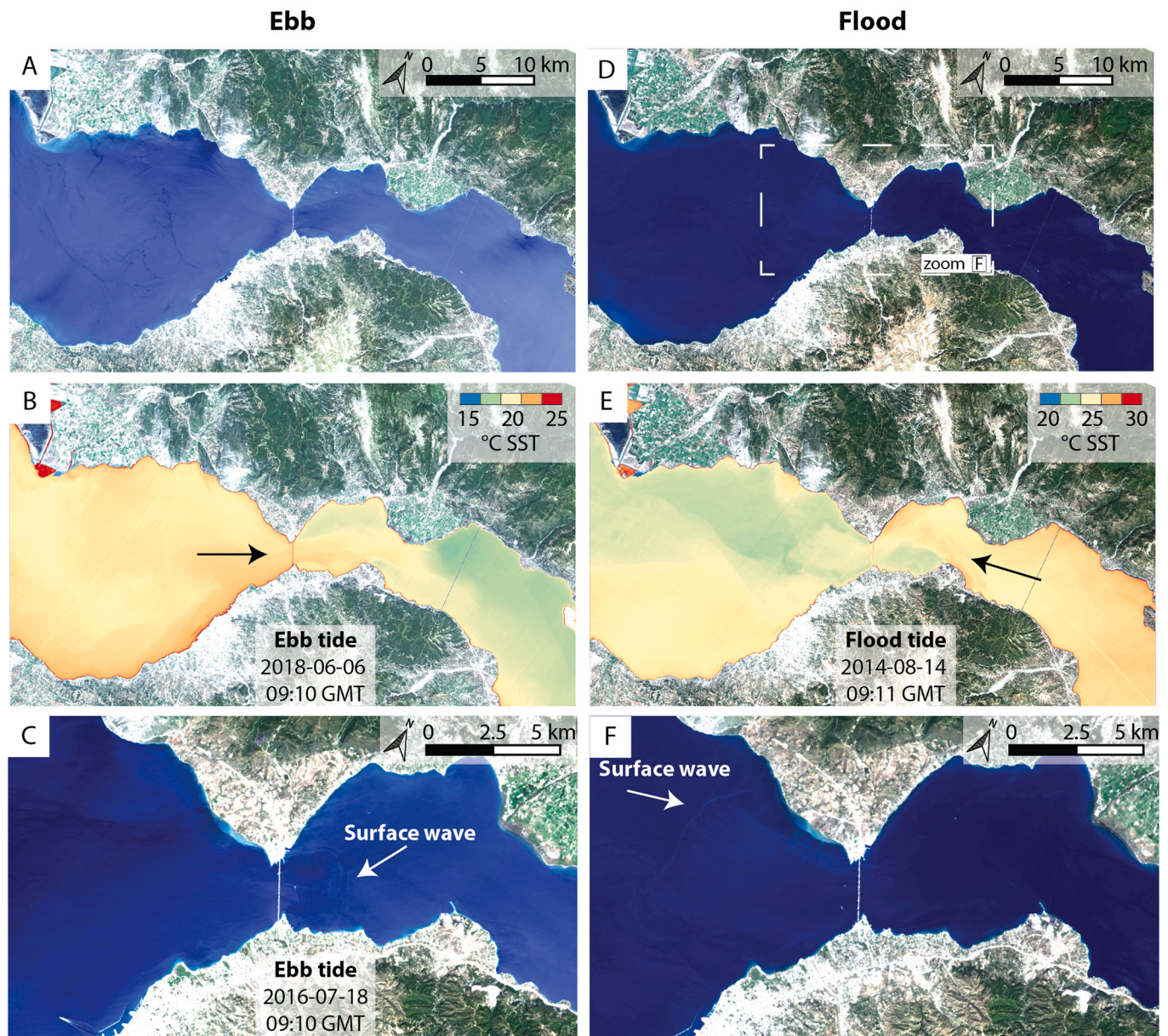
Ebb

Flood

Fig. 4. Landsat 8 optical (A, C, D, F) and thermic (B and E) images during ebb tide (A, B, C) and flood tide (D, E, F).

Horsch (2015) modelled the Nafpaktos upwellings as the result of tidal circulation and/or SW wind.

4.2. Currents

The current circulation is based on a single ADCP survey in May 2019 with tidal coefficients from 52 to 96 and tidal range from 0.2 to 0.5 m for the Patras location (data from tide tables produced by the NOAA/ National Ocean Service). During spring tides, the tidal range can reach 0.8 m. The tidal analyses are based on the sea level variations in the Mediterranean Sea, here in the Patras Gulf.

Fig. 5 shows a close correlation between the tides and the direction of the currents in the Rion strait-center zone (Fig. 2). During the ebb (negative slope tide) the currents flow north-eastward (Fig. 5). Moreover, on satellite optical images, we can identify a surface wave located at 3 km from the Rion Strait moving in an eastward direction (Fig. 4C). At the opposite, during the flood (positive slope tide), the currents flow south-westward (Fig. 5), and a surface wave was observed on a satellite image at 7 km from the strait travelling in a westward direction

(Fig. 4F).

The water volumes exchanged between the Corinth and Patras Gulfs during a tidal cycle are estimated by integrating the current velocity on the strait section as well as ebb and flood times from ADCP data (Table 1). We obtain 1.08 km^3 of water for the ebb tide and 0.90 km^3 for the flood tide (see the parameters in Table 1). Consequently, the timing and direction of the currents in the Rion strait-center shows a tide-dominated strait with a semidiurnal tidal cycle.

4.2.1. Ebb tide

The tidal ebb flow enters from the Patras Gulf to the Corinth Gulf, i.e. from West to East (Figs. 5, 6). The ebb consists mostly in surface currents (Fig. 7) speeding up in the strait area with velocity up to 1 m/s (Fig. 6). This amplification of the tide by the strait constricted morphology is a common process (e.g. Gibbard, 1995). The ebb flow strongly interacts with the northern and southern shallow seafloor in the Rion strait-center zone (Figs. 6, 7). This warmer ebb current extends until the Drepano spit in the Nafpaktos zone (see location in Fig. 2, currents in Fig. 6) andenters in the colder Corinth Gulf (Figs. 3, 4B), with a volume of ~1 km^3
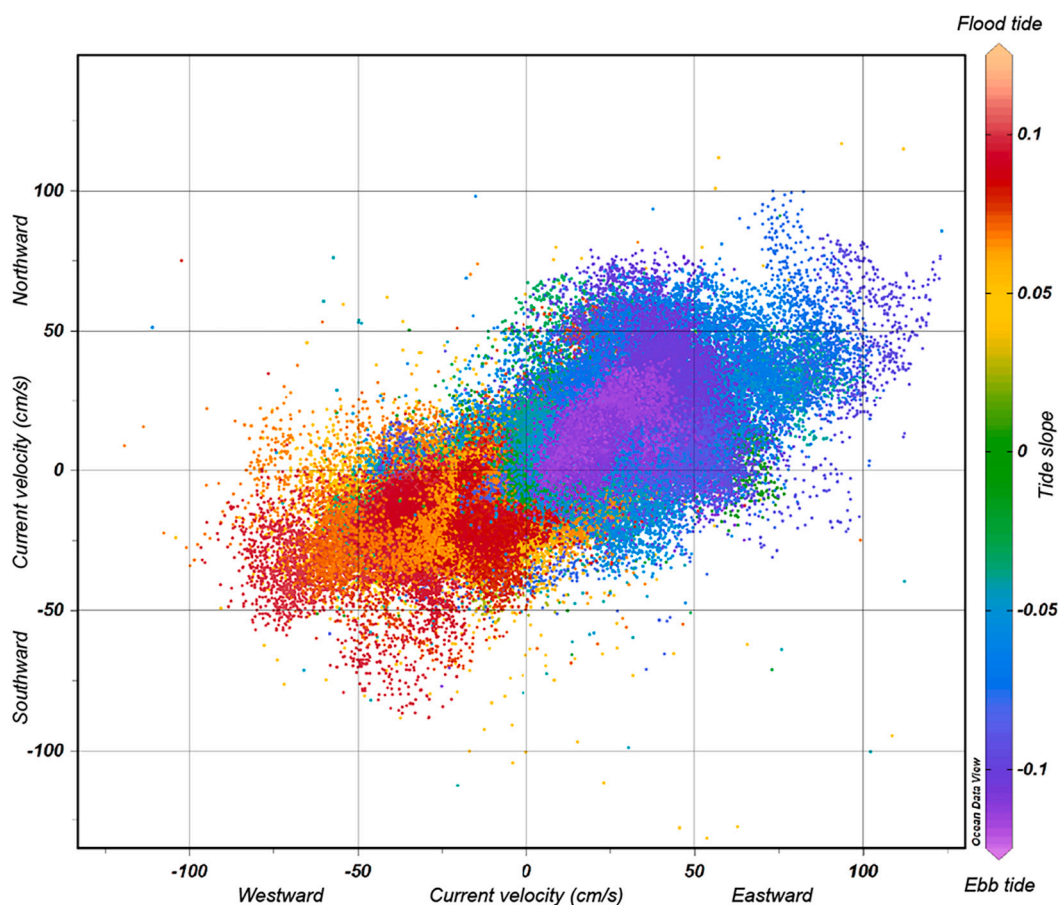
Fig. 5. Current direction vs tide slope based on ADCP data in the Patras, Rion and Nafpaktos zones. The slope tide is the derivative of the high tide with respect to time, giving a numeric parameter for ebb or flood tide.

Table 1
Tidal water volumes passing through the strait obtained from the use of an Acoustic Doppler Current Profiler (ADCP).

	Ebb	Flood
Strait section (m^2)	8.32E+04	
Duration (s)	16,200	10,800
Current velocity (m/s)	0,8	1
Volume (m^3)	1.08E+09	8.99E+08

(Table 1).

Looking in more details at the characteristic of the ebb water flow pattern, we observe along the East-West ADCP profile in Fig. 8, a two-layer water system with the upper ebb current layer going into the Corinth Gulf and a bottom layer flowing in the reverse direction from the Mornos zone to the Nafpaktos zone.

The bottom flow is locally significantly faster, up to 3 m/s, and more turbulent than the surface ebb flow that is slower than 1.5 m/s (Figs. 6, 8). The thickness of the bottom current layer can reach 50 m above the seafloor (Fig. 8). It is important to note that these bottom currents stay restricted in the Mornos and Nafpaktos zones and do not reach the strait.

4.2.2. Low tide
From the ebbing to flooding stage, the current velocities are very slow (slack water) with less than 0.5 m/s, except for the bottom currents which flow eastwards with velocities up to ~1 m/s (Supp. Fig. 16). These bottom currents are still restricted to the deepest part of Nafpaktos bay with a thickness smaller than ~20 m. At the surface, the Nafpaktos and Mornos zones share the same current pattern, eastward currents

along the northern coast and westward ones along the southern coast.

4.2.3. Flood tide
During the flood tide, i.e. positive slope tide, the currents flow southwestward out of the Corinth Gulf (Figs. 4, 5, 6). In the Patras zone, the currents, especially the bottom ones, are stronger along the southern shore (Fig. 6). In the Rion strait-center zone, the currents show the fastest velocities ranging between 0.6 and 1 m/s (Figs. 6, 9A).

The N-S ADCP profile in the Rion strait-center zone shows that the flood currents are mainly bottom currents localized in its center and flowing out to the South-West with velocity up to 1 m/s (Fig. 9A). The northern and southern shores show no significant water motions (Fig. 9A).

The E-W ADCP profile in Fig. 10A depicts a two-layer system: at the surface, a west to east current layer flowing with velocities ranging from 0.2 to 0.6 m/s; near the bottom, an east to west current layer flowing with very high velocities up to 3 m/s in the Nafpaktos Bay. The two layers are separated by a 30-40 m deep interface and are strongly interacting at the Rion strait-center zone with the possible triggering of an internal wave, or internal hydraulic jump which may reach the surface (Figs. 4, 10A; e.g. La Violette and Arnone, 1988; Pistek and La Violette, 1999; Sánchez-Garrido et al., 2011; Hilt et al., 2020). Moreover, the bottom current layer extends over the strait but remains restricted to its deeper part (Fig. 10A). These bottom currents originating from the Corinth Gulf can cross the strait and reach the Patras zone (Fig. 6).

4.2.4. High tide
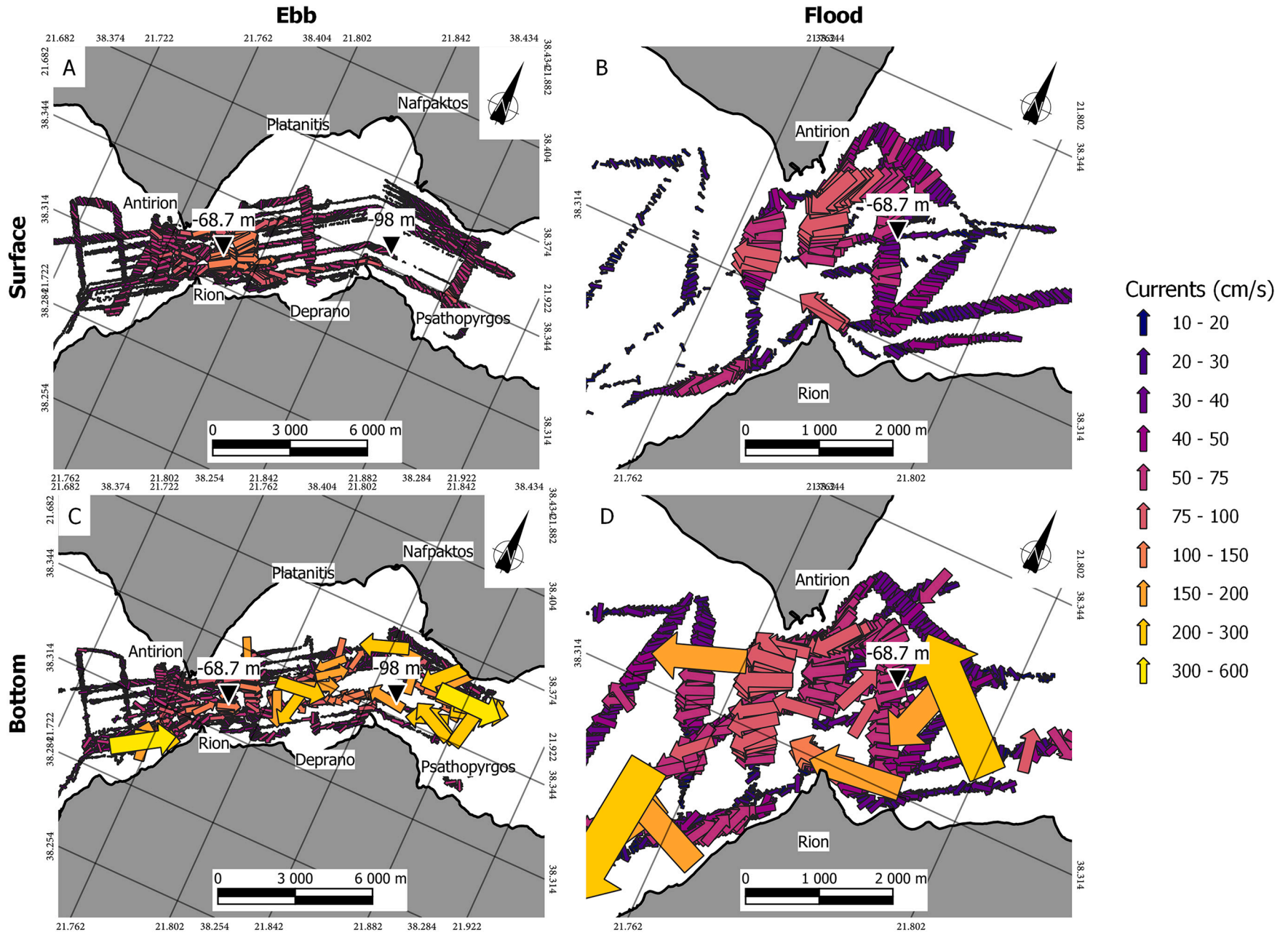From the flooding to ebbing stage, we also observe the two-layer

Fig. 6. Current map during ebb tide (A, C) and food tide (B, D) with surface currents (A, B) and bottom currents (C, D). The length and width of the arrows are scaled with the current velocity and the map scale.
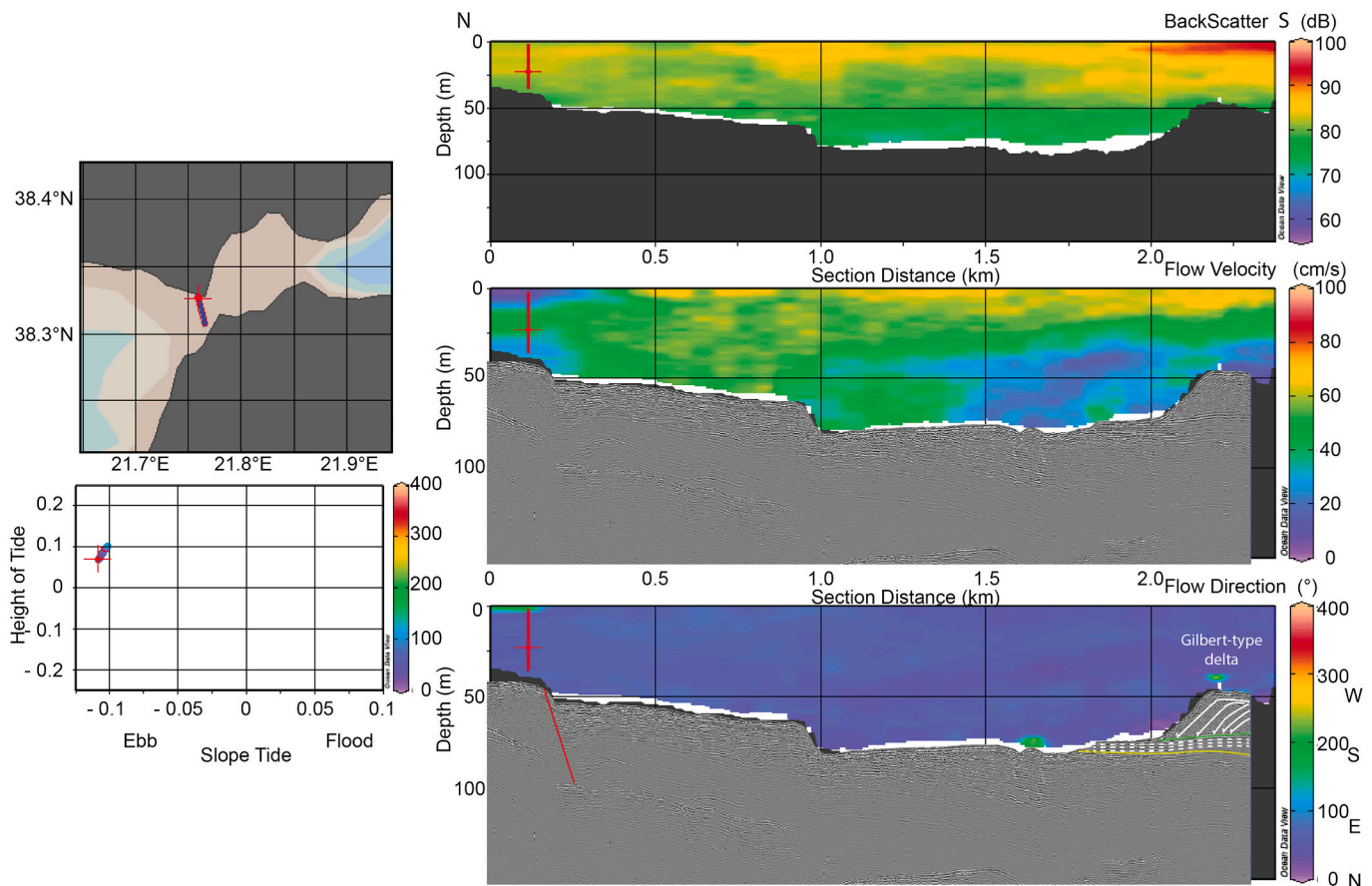
Fig. 7. North-South cross-section in the strait-center area during the ebb tide with back scatter, current velocity and current direction with a sparker seismic profile on the right, and on the left the location of the profile and the slope tide vs height of tide.

stratified system (Supp. Fig. 17). The surface currents are going from west to east with velocities between 0.4 and 0.8 m/s. The bottom currents flow in the same direction with higher velocity (2 m/s; Supp. Fig. 17).

4.2.5. Circulation summary and interpretations

The documented circulation represents specific conditions in terms of tides, wind, SST, among others. We assess important seasonal and interannual variations due to tidal and meteorological conditions (Candela et al., 1989; García Lafuente et al., 2007).

Based on the open Mediterranean Sea level variations in the Patras Gulf, the 'flood' and 'ebb' tidal components are opposite to the 'usual' tidal components in straits. Indeed, the flood current in a strait is represented by tidal phase directed towards the smaller or more oceanographically enclosed basin, that is internal with respect to the open ocean (Defant, 1961). This definition is only relative to the current directions and does not consider the tidal sea level variations of the area, nor the local oceanographic settings like among other the amphidromic points or the internal tides. This study case shows a possible misleading between the 'flood' with currents toward the Gulf of Corinth during the 'ebb' of the sea level on each side of the strait (Supp. Fig. 19). To explain this current circulation, we can consider the characteristics of the two connected basins: the Gulf of Patras is a very shallow area with a maximum depth of ~100 m and small with a surface of 350–400 km^2 connected with the Mediterranean Sea. On the other side, the Gulf of Corinth is a very deep ~1000 m water depth and a larger area of 2400 km^2. This singularity is well shown on the Fig. 1 and may impact the current pattern.

The ADCP profiles thus depict a two-layer water system with a complex dynamic summarized in Table 2. The surface layer current

directions are well correlated with tides with the usual semidiurnal tidal frequency. The bottom layer has higher velocities currents from the Nafpaktos-Mornos zones, and can share the same or opposite current directions as the tidal surface layer currents (Table 2).

These bottom currents can flow over the Rion strait-center zone and reach the Patras zone (Figs. 8A, 10A, 16, 17 and Table 2). On several ADCP profiles, we observe that the bottom current velocities are decreasing westward. Here we interpret these bottom currents in relation with the internal waves coming from the cold and deep Corinth Gulf with a tidal quarter diurnal frequency (~6 h). As defined by Shepard (1975) these internal waves at a tidal frequency are internal tides. This process is associated with eddies and strong turbulences impacting the seafloor as well as some upwellings identified by cold SST located near the Mornos Delta (North Fig. 4) or around the Drepano spit along the southern shore (Fig. 4). These upwellings have already been reported by Lascaratos et al. (1989) and modelled by Fourniotis and Horsch (2015) but they were interpreted as wind-driven upwellings except along the northern coast of the Nafpaktos Bay. Our observation suggests that the upwellings could be generated by the internal tides.

During ebb tide, we observed the warmer surface waters from the Patras Gulf entering the Corinth Gulf. This incoming warmer volume reinforces the contrast between the surface and deep waters. At the same time, we observed a fast reverse direction bottom current from the East to the West restricted in the deeper parts of the Mornos and Nafpaktos zones (Fig. 10, Table 2). We interpret these bottom currents as "low-energy": they do not overspill the strait and thus stay restricted to the Corinth Gulf by breaking on the western tip of the Nafpaktos Bay. We called it a low-energy high internal tide (Fig. 14). During the ebb to flood tide transition (Fig. 16), the direction (to the east), the velocity (1 m/s) and the thickness (20 m) of the bottom layer are interpreted as the
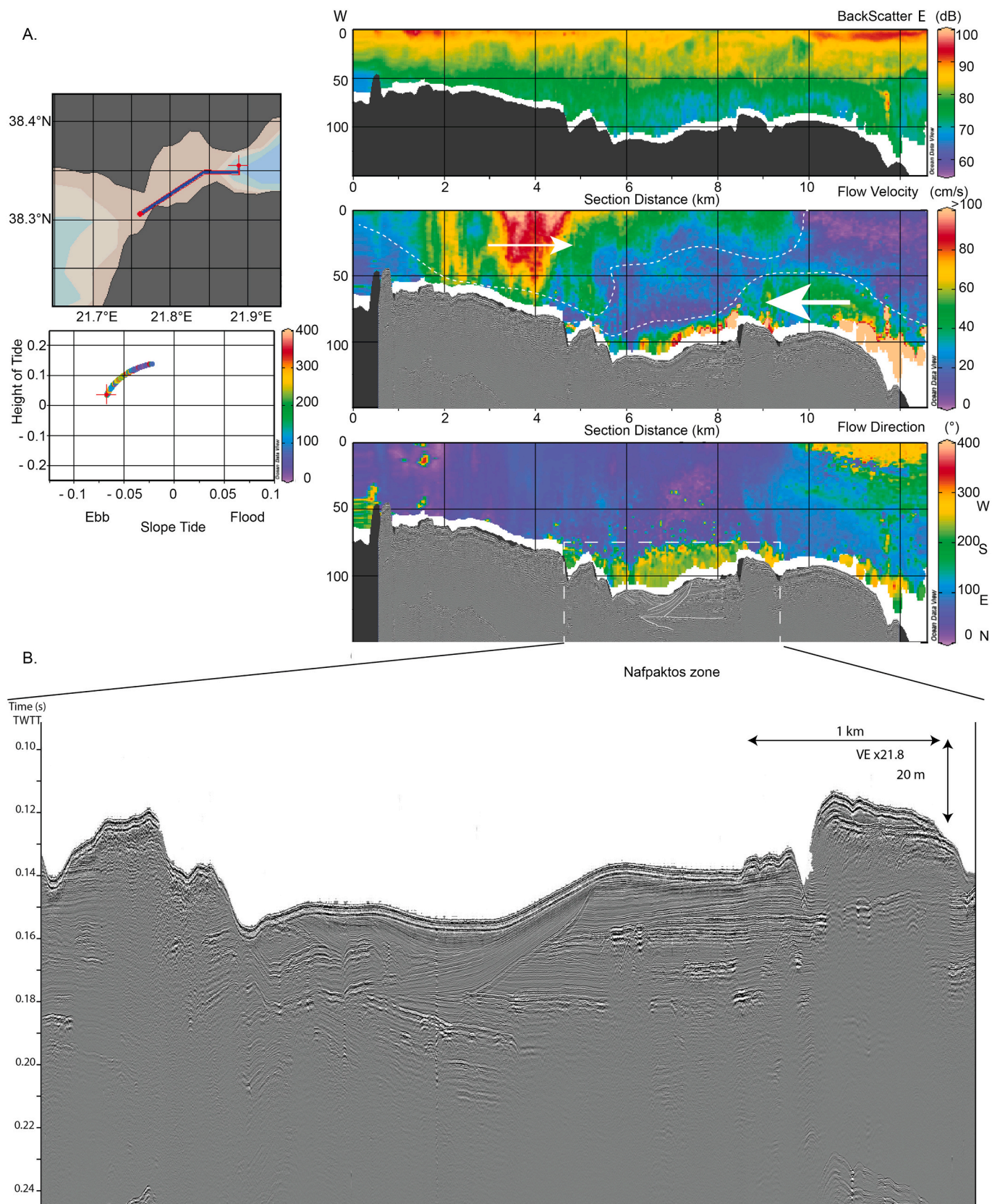
Fig. 8. A. West-East longitudinal section along the strait during ebb tide with back scatter, current velocity and current direction on the right, and on the left the location of the profile and the slope tide vs height of tide; and B. zoom on the sparker seismic profile at the bottom.
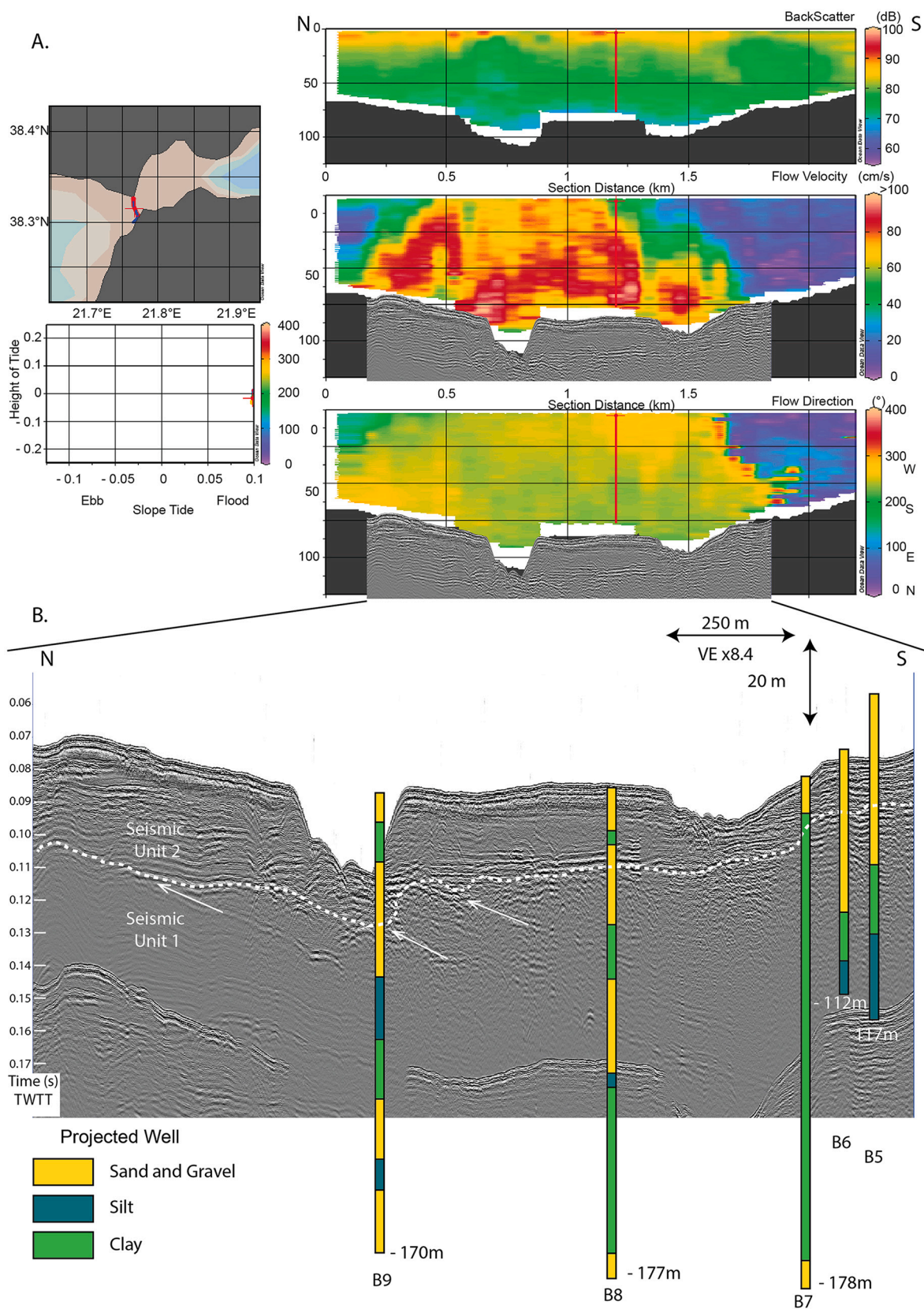
Fig. 9. A. North-South cross-section in the strait-center area during flood tide with back scatter, current velocity and current direction on the right, and on the left the location of the profile and the slope tide vs height of tide; and B. sparker seismic profile with the projected bridge pillar drillings from Yang et al. (2001).
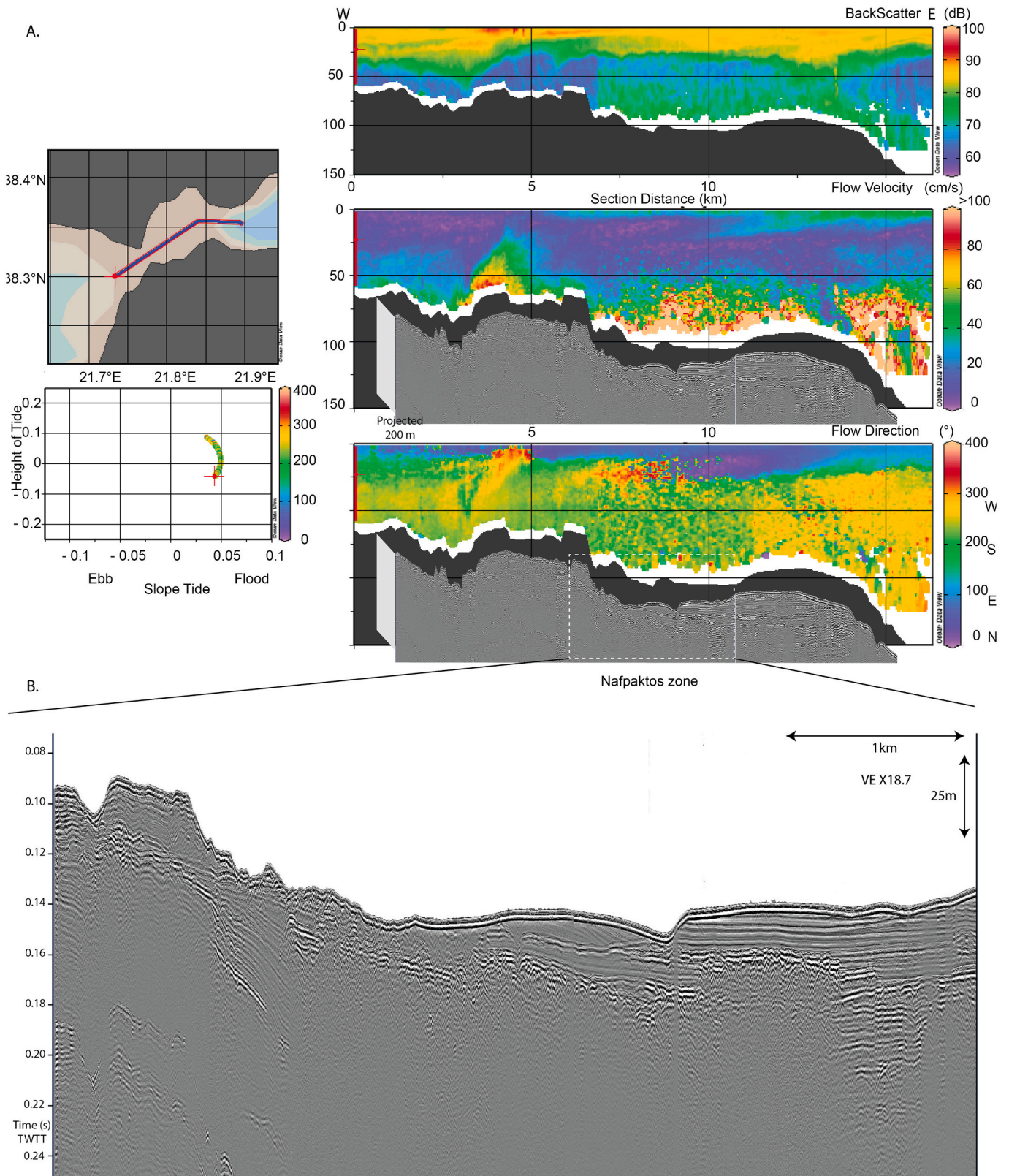
Fig. 10. A. West-East longitudinal section along the strait during flood tide with back scatter, current velocity and current direction on the right, and on the left the location of the profile and the slope tide vs height of tide; B. projected sparker seismic profile.

recede of this internal tide (Fig. 14). During the flood tide, strong currents are flowing out of the strait, i.e. with a south-westward direction (Figs. 5, 6). The flood current consists of bottom currents with velocities decreasing westward (Fig. 9). We interpret these bottom currents as the

release of the potential buoyancy formed during the ebb tide by the input of large volume of warmer surface waters from the Patras Gulf. We interpret these bottom currents as "high-energy" because they flow out of the strait. We call this stage a high-energy internal tide (Fig. 14).

Table 2
Current direction comparison between tide current and inter-tide based on tide cycle.

Time	A	B	C	D	E	F	G	H
Tidal currents		Ebb tide		Ebb to flood tide transition		Flood tide		Flood to ebb tide transition
		Eastward (surface)		Westward		Westward		Eastward
Internal tide (bottom)		Westward		Eastward			Westward	Eastward
		Opposite	Same		Opposite		Transition	Same

During the flooding to ebbing, the surface and bottom currents share the same eastward direction (Fig. 17). The strait currents have a low velocity despite bottom current velocity reaching 2 m/s. We interpret this stage as the recede of the high-energy internal tide.

To summarize, we suggest that the water circulation is driven by an ebb flow of warm surface waters from the Patras Gulf into the Corinth Gulf. This flow disrupted and enhanced the potential buoyancy at the interface of the two water masses in the Corinth Gulf, which releases its energy forming an internal tide. The internal tide has a higher frequency than the tide with at least two breakings during a tide cycle. Indeed, we infer a maximum period of ~6 h for the internal tide. Hence, we hypothesized that: (1) a higher-energy internal tide flows out of the strait during the flood tide; and (2) a lower-energy internal tide stays restricted in the Nafpaktos bay during the ebb tide (Fig. 14).

4.3. Bathymetry and morphology of the strait bottom

4.3.1. Rion strait-center zone and sill bathymetry

The Rion strait-center zone consists of a plateau at a bathymetry ranging between −60 and −70 m bounded by steep northern and southern slopes (Fig. 11A). The faults identified from the sparker seismic profiles do not affect the morpho bathymetry of the strait: there is no significant surface offset. However, two morphologies are influenced by faulting and then reshaped by the tidal currents: the channel (see Table 3) and the terrace at the Northwest.

We identify two platforms at the depths of −20 m and − 30 m on the northern side, and a less well defined one at the depth of −20 m on the
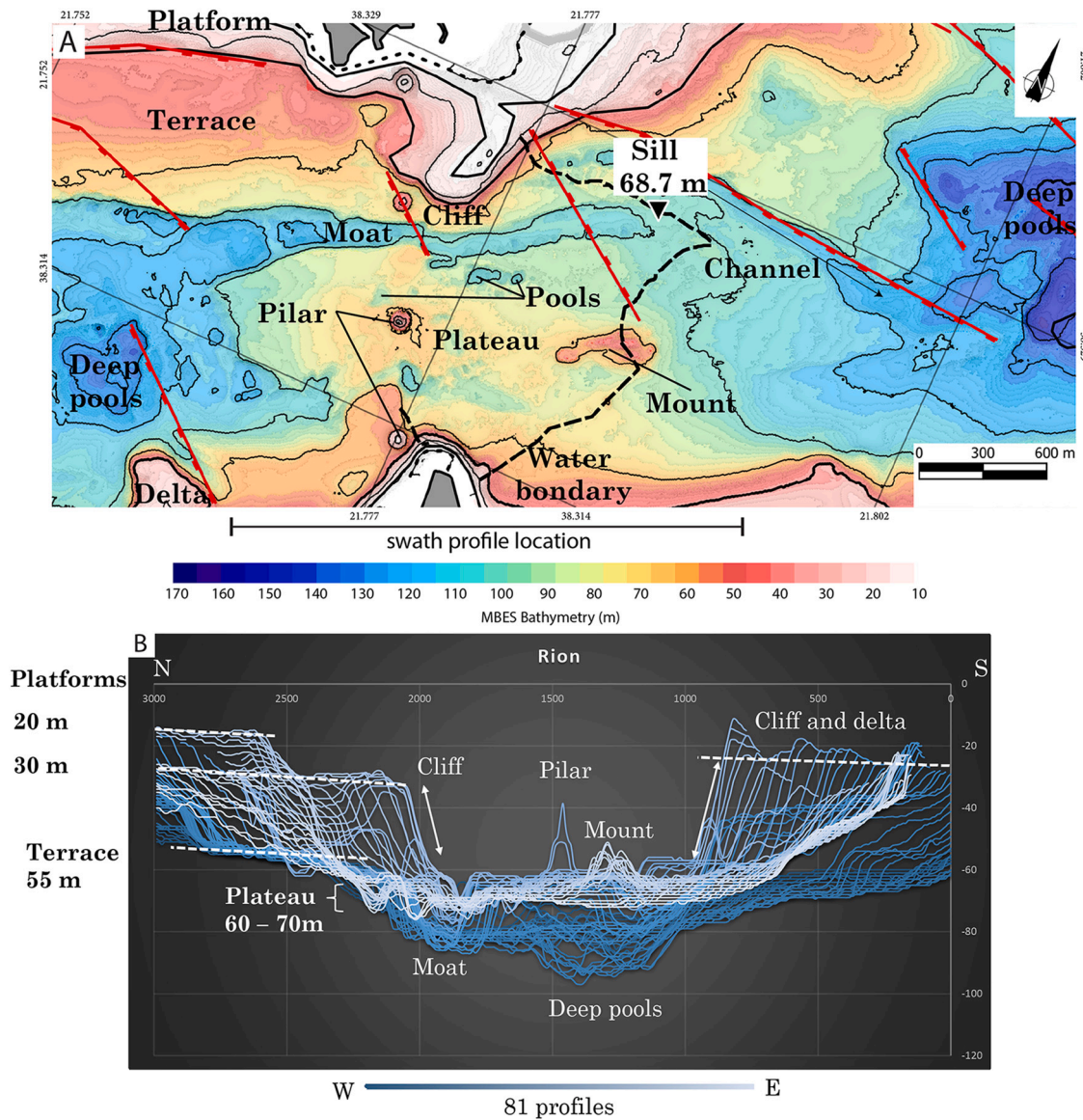

Fig. 11. A. Rion strait-center zone morpho-bathymetry and B. N-S swath profiles with dark blue for western profiles and light blue for eastern profiles. (For interpretation of the references to colour in this figure legend, the reader is referred to the web version of this article.)

Table 3
Morphological comparison between Rion strait-center moat and channel.

	Moat	Channel
Direction	N65	N95
Length	2 km	1,6 km long
Width	140 m (NE) to 240 m (SW)	100 m (W) to 270 m (E)
Depth	3 m (NE) to 21 m (SW)	4 m (W) to 6 m (E)
Sinuosity	1.0	1.0
Slope	- Plateau 0.07° (0.13%) Patras 0.64° (1.12%)	0.69° (1.21%)
Width/depth ratio	14 (Plateau) to 47 (Patras)	26 (W) to 43 (E)
Shape	U-shape, symmetric	V-shape, asymmetric left bank (N) is 5 m upper than the right bank (S)
Process	Moat digs by tidal bottom currents	Fault relative stream channel from coast to basin

southern side (Fig. 11B). The northern and southern margins of the strait form nearly vertical 30 to 40 m high cliffs. In between, a plateau at −60 -70 m depth constitutes an irregular and rough surface. The underwater videos above the western part of the plateau show a rough rock-paved surface encrusted by living red corals and sponges (see location on Fig. 2A). The plateau exhibits several morpho-bathymetric features: a mount, several pools, a moat and a channel that are described below.

The mount is located near the eastern part of the plateau area (Fig. 11). It is an elongated 420 m long and 150 m wide mount standing 15 m above the plateau. The elongation direction shows a N65 trend (Fig. 11). The pools are mainly located in the central part of the plateau. They form −5 m to −10 m deep incisions in the plateau surface. The pools are mainly elongated with long / wide ratio of 2 to 3 with dimensions of 150 to 350 m long and 80 to 120 m wide. They present the same N65 direction as the mount (Fig. 11).

The moat is located in the northern part of the plateau and does not extend outside. It is a nearly straight 2 km long and 140 m (E) to 240 m (W) wide channel. Its incision in the plateau increases from East to West respectively from −3 m to −21 m with a width/depth ratio of 14 to 47 (Table 3, Supp. Fig. 18). The moat shows an overall U-shape with steep edges, a rough bottom (Table 3, Fig. 18). The moat strikes N65 and its slope is 0.07° (0.13%), but this value is poorly consistent (R2 = 0,14) due to the chutes-and-pools morphology (Fig. 18). In addition, the moat slope changes at the location of the edge of the plateau where they are steeper slopes of 0.64° (1.12%) (Fig. 18). This moat is parallel to the coasts and is not associated with any river mouth on the coast. The moat north-eastern tip corresponds to the plateau edge and localizes the Rion sill at a depth of 68.7 m (Fig. 11). The strait bathymetry in its narrowest part, i.e. below the Rion-Antirrion bridge, has a maximum depth of −72 m within the moat.

In contrast, the channel is located in the eastern part of the plateau (Fig. 11). It is straight, 1.6 km long, 100 m wide in the West and 270 m wide in the East and a respective width/depth ratio of 26 and 43 (Figs. 11, 18 and Table 3). The channel extends from the steep northern slope break at the depth of −70 m to the Nafpaktos Basin at the depth of −93 m and its 0.7° (1.2%) slope is rather constant (Table 3 and Supp. Fig. 18). The channel cuts in the plateau with a N95 direction (Fig. 11). In the swath profiles along the channel, we observe that its northern edge is 5 m higher than its southern one (Fig. 18). On the high-resolution seismic profiles, we identify a normal fault that bounds the channel on the North (Fig. 11). This channel is intrinsically different from the bottom current generated moat. Indeed, this channel shows all the characteristics of stream channel, i.e. formed by a fluvial process on a slope, in this case 0.69° (1.2%) (Table 3, Fig. 18).

4.3.2. Patras zone

The Patras zone starts west of the plateau and moat with a deep rough area consisting of deep pools and deep crests (Fig. 2). The Patras zone is a complex basin, affected by deformation and generally characterized by the lack of sediment deposition (Fig. 12). We used an observed ridge to subdivide the zone in two sub-areas: the South-West (SW) mini basin and the North-East (NE) mini basin (Fig. 12A). This ridge is curved with a N100 strike in the North and a N320 strike in the South, and is the locus of the Patras sill at 50 m water depth. The ridge is wider and higher at its tips, and narrower and thinner in its center. On the sparker profile (in Fig. 12C), we observe that the ridge is the result of the interaction between an active push up structure and the marine bottom current erosion.

The SW mini basin consists of a circular depression with no recent sediment deposits. The NE mini basin is shaped by deep pools limited by deep crests, hereafter referred to as pool-and-crest morphology (Fig. 12). This NE mini basin is bordered to the North by stepped terraces at depths of −60 m, −54 m and −36 m (Fig. 12B). The orientations of the terraces are similar to the one of the moat, i.e. N70 (Fig. 12). The terraces are 2 km long and 400 ± 50 m wide (Fig. 12). The southern shore is very steep and reveals the occurrence of a Gilbert-type delta, 840 m long, 320 m wide and 30 m high (Figs. 7, 12). The foreset direction of progradation is from South to North. The topsets are located at the depth of −40 m and forms a platform. Moreover, a terrace is observed on the southern shore at a depth of −60 m between the Gilbert-type delta and the Rion sill. The center deep area in the NE mini basin consists of deep pools of two types: elongated in the northern part, and sub-circular in the southern part (Fig. 12). The elongated deep pools are located in front of the moat outlet and display a N68 long-axis strike, similar with the moat direction. These deep pools reach a depth of – 80 m (Fig. 12). The southern sub-circular deep pools are deeper and can reach – 93 m of depth. They are bordered by narrow crests, 50 m to 80 m wide forming irregular 20 m high walls. The pools diameters range from 100 m to 340 m (Fig. 12).

4.3.3. Nafpaktos zone

The Nafpaktos bay is 7 km long with a N64 strike (Figs. 2, 13A). Its width is larger than 7 km from coast to coast and the bathymetry at its center reaches −119 m (Figs. 2, 13A). The Nafpaktos zone starts East of the plateau characterizing the Rion strait-center zone and ends at the deepest Nafpaktos-Mornos sill at −98 m depth, between the Drepano spit and the Mornos delta (Fig. 13A).

The Nafpaktos zone is characterized by a gentle northern slope of 3° (2.8%) and by a steep southern slope of 5.4° (9.5%, Fig. 13B). The bathymetry, the swath profiles and the sparker seismic profiles show that the northern slope is veneered with thin sediment beds migrating up-slope (Fig. 13A and B).

The western part of the Nafpaktos Basin outlines deep pools at a depth of −90 m with an average size of 300 m and an incision of −10 m. They are sub-rounded to elongated (Fig. 13A). These pools are localized at the tip of active normal faults at the transition between the Rion plateau and the Nafpaktos zone (Fig. 13A).

The central and deeper part of Nafpaktos Basin is formed by smoother features: a giant pool and a gutter. The giant pool has a bathymetry deeper than −110 m. It is 1600 m long and 850 m wide and shows a N59 strike (Fig. 13). Northwards, the gutter is a 560 m long and 70 m wide depression with a N81 strike. It forms a narrow U-shaped 8 m deep erosion reaching the depth of −115 m (Fig. 13).

The sparker seismic profiles in the Nafpaktos Basin show a large-scale active erosional and depositional feature with km long wave-length and tens of meters deep scouring (Figs. 8B, 10B, 16). Their internal structures show a large-scale cross-bedding with 3 km long wavelength and 25 m amplitude (Figs. 8B, 10B, 16).

4.3.4. Mornos zone

The transition between the Nafpaktos and Mornos zones is a deep narrow U-shaped constriction of 450 m wide between the Mornos Gilbert-type delta to the North and the Psathopyrgos-Drepano Gilbert-type delta to the South. It forms the Nafpaktos-Mornos sill with a depth of −98 m (Figs. 2, 13). No active faulting is evident in the area.
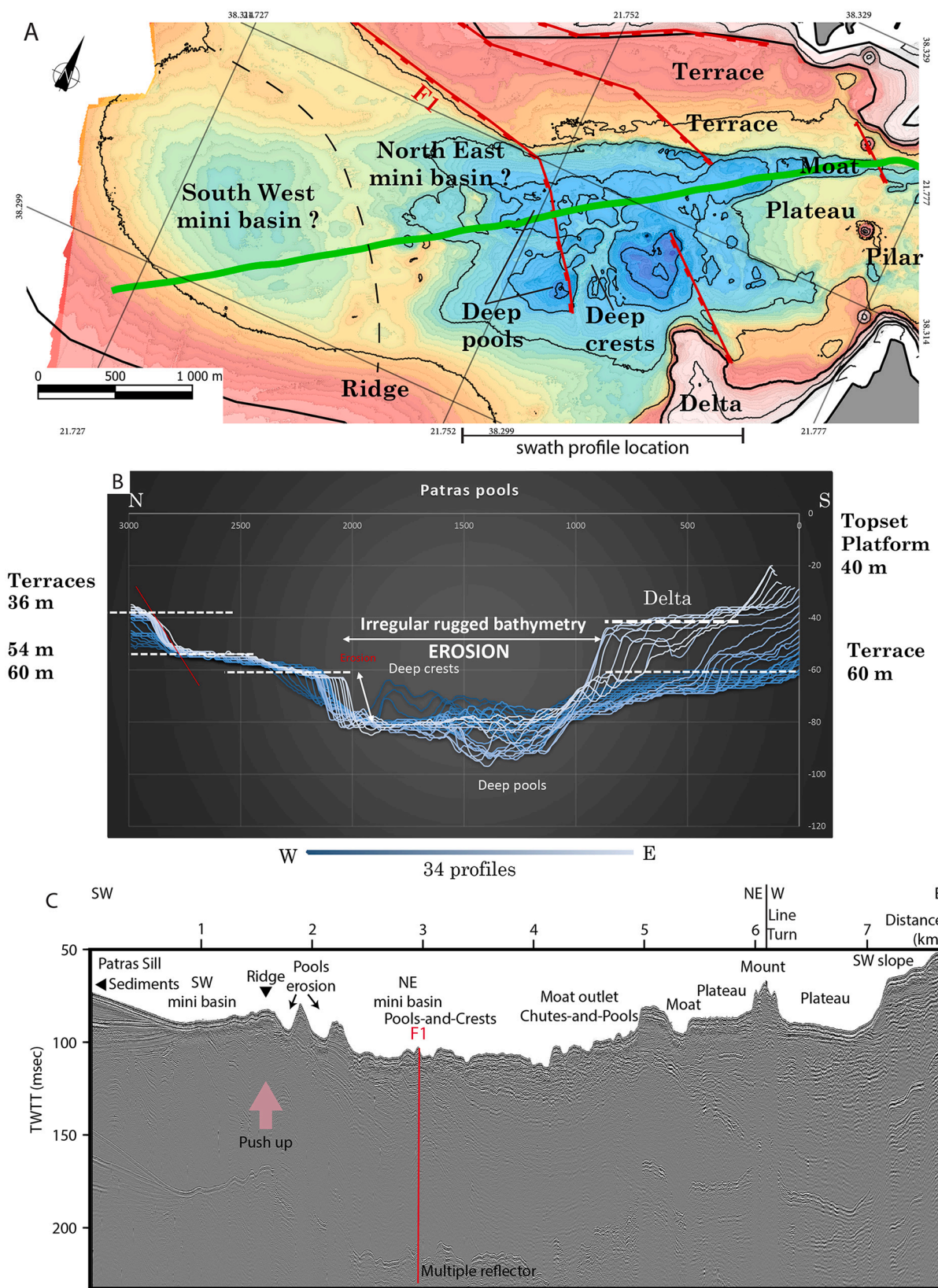
Fig. 12. A. Patras zone morpho-bathymetry, B. swath profiles on the pool-and-crest area (NE mini basin) and C. sparker seismic profile located by the green line on Fig. 12A and on Fig. 2A. (For interpretation of the references to colour in this figure legend, the reader is referred to the web version of this article.)
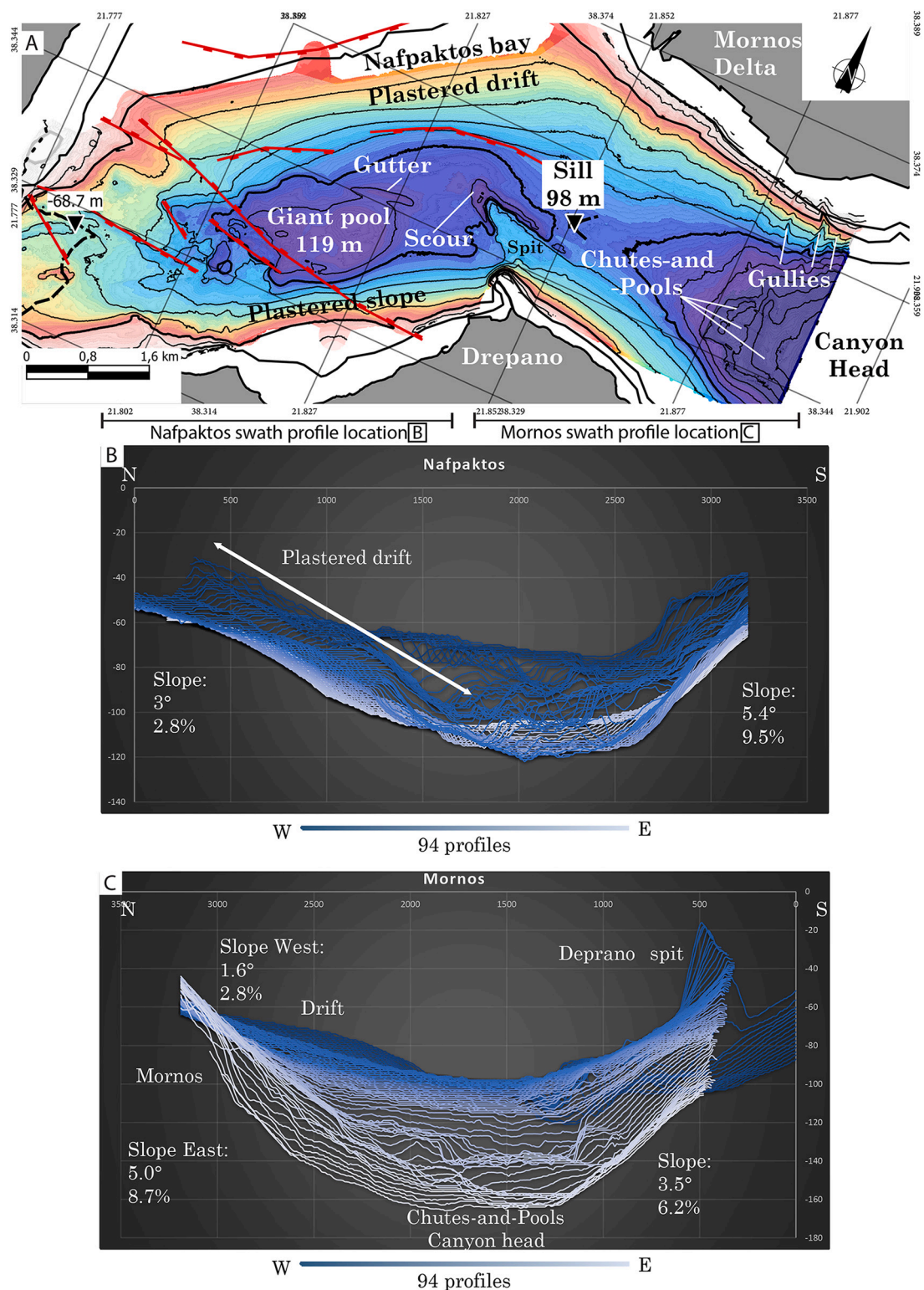
Fig. 13. A. Nafpaktos zone and Mornos zone morpho-bathymetry; B. swath profiles with plastered drift on the north shore and plastered slope to the South; C. swath profiles with plastered drift on the drift and the Mornos Gilbert-type delta on the North, and the Drepano spit on the south.

On the southern shore, we pinpoint the Drepano spit which was identified by Piper et al. (1980). This spit strikes N130. It consists of a shallow coastal body ranging in depth between 0 m and − 50 m, bordered by very steep slopes. Offshore, we identify a deep spit, below −80 m of depth, in front of the onshore one. The offshore spit is outlined by scours (118 m) at its base (Fig. 13). To the West, the spit edge is a

nearly vertical 34 m high scarp perpendicular to the southern Nafpaktos coast, and to the East, the spit edge is less steep and parallel to the Drepano coast (Fig. 13). The onshore and offshore spits are localized at the change of the orientation of the coastline trend between the Nafpaktos zone (N62) and the Mornos zone (N90). Thanks to the ADCP analyses and Landsat 8 images, we know that this spit is also located at

the limit between warmer surface currents and upwelling of colder waters related to the internal tides (Figs. 4, 6, 8, 10).

On the opposite northern coast, the slope of the Mornos Gilbert-type delta increases eastwards from 1.6° (2.8%) to 5° (8.7%; Fig. 13A). Moreover, its eastern slope is affected by gullies on the delta front (Fig. 13). The current analyses and the SST document an upwelling along the eastern front of the Mornos Gilbert-type delta (Fig. 4).

The eastward deep part of the Mornos zone displays a chute-and-pool geometry at the head of the Mornos canyon which connects the Mornos zone with the Corinth Gulf deep basin (Beckers et al., 2016; Fig. 13). The chutes-and-pools have a wavelength ranging from 100 m to 500 m and an amplitude between 10 and 20 m (Fig. 13). The Mornos zone is also affected by high velocity bi-directional bottom currents (Figs. 6, 8). The sediments from the western part of the Mornos Delta are reworked by bottom currents.

4.3.5. Bathymetry and morphology interpretations

In the Rion Strait center zone, we interpret the plateau, the mount, pools, and moat as erosive morphologies. These morphologies share the same direction as the bottom currents (N65). Indeed, the Rion strait-center zone is swept by the tidal currents, mainly during the flood tide, and by the internal tide outflows. The velocities, up to 1 m/s, are high enough to erode up to coarse-grained sands (Stow et al., 2009). In the moat, the chutes-and-pools can be referred to super-critical flows which could generate hydraulic jumps (Cartigny et al., 2014). We interpret the channel low sinuosity, its direction, and the systematic elevation shift between the channel edges as related to its faulting. Moreover, the channel is interpreted as inherited from the last glacial lowstand. It erodes the slope and enters the isolated Nafpaktos/Corinth Lake.

In the Patras and Nafpaktos zone, the irregular rugged bathymetry characterized by a lack of sediment deposits is interpreted as the product of turbulent bottom currents probably carrying coarse-grained sediments. A key point in these areas is the absence of any sediment deposition evidenced by seismic reflection profiles. It is a net erosional area which implies that the pools and crests result from erosional bottom currents (Fig. 12). We interpret the deep pools, the giant pool, the gutter, the large-scale scouring as the result of erosion by turbulent bottom currents. We assume that that the bottom currents are generated by the breaking of the internal tide or the shoaling transformation stage (sensu Shanmugam and Wang, 2014) from the Gulf of Corinth on the sea floor. The breaking of the internal tide would trigger eddies and hydraulic jumps which are scouring the seafloor (Figs. 8B, 10B, 13).

In the Nafpaktos zone, we agreed with Beckers et al. (2016) interpretations for the northern slope as a plastered drift and built by the bottom currents. The southern slope is interpreted as a plastered slope, i. e. with higher slope and lesser sediments than the northern slope. In the Mornos zone, the Drepano spit is interpreted as the connecting area where two water masses, i.e. the surface ebb flow and the cold bottom upwelling, are mixed due to the change in direction of the bay (Figs. 4, 6). In the canyon head, the chutes-and-pools are related to the evidenced high velocity bottom currents. The maximal recorded velocity in the canyon head is up to 6 m/s (Figs. 6, 8).

Surprisingly, despite the proximity of two giant Gilbert-type deltas, the bottom currents are strong enough to erode the sediments to maintain the connection between Nafpaktos Bay and the Corinth Gulf. The connection morphology displays a deep narrow U-shaped constriction, 450 m wide. Indeed, the km-scale of these giant Gilbert-type deltas and their relative sediment supplies in a such narrow area, without evidence of active normal fault, would usually lead to the quick overfilling of the bay. This observation reinforces the key roles of the bottom currents of the internal tide as the main process in this area which rework huge volumes of sediments.

5. Discussion

5.1. Morphologies and grain size

In order to describe the sedimentary system, we remapped 185 grab and short core samples in the Patras Gulf (Piper and Panagos, 1979), in the Rion Strait (Piper et al., 1980) and in the Nafpaktos Bay (Beckers et al., 2016). We complete this review with our underwater camera data. The grain size for each morphology is presented in Table 4.

The deep Patras zone, i.e. the pool-and-crest area, is filled with gravelly sand, largely with a biogenic origin, which includes some pebbles (Piper and Panagos, 1979). The grain size decreases westward to gravelly mud and slightly sandy mud (Piper and Panagos, 1979).

The pool-and-crest morphology is interpreted as the result of high velocity bottom currents carrying pebbles and granules, which erodes the pools and sweep the crest. The interaction of dense flows with submerged topography leads to the formation of lee waves and eddies strongly interacting with the seafloor (e.g. Hilt et al., 2020). By symmetry with the strait, we suppose that the same morphology in pools and crests located on the east side of the strait is built by similar processes and made of the same grain size (Table 4). Schematically, the Patras pools and crests are shaped by the outflow of the flood internal tide, and the Nafpaktos pools and crests are dug by the ebb internal tide (Fig. 14).

The terraces in the Patras zone show a grain size increasing with depth. Indeed, the shallower terrace at 36 m is composed of silty mud deposits whereas the middle terrace at 54 m displays a gravely mud and slightly gravelly sandy mud-covered surface and the deepest terrace at 60 m is veneered by gravelly sand largely biogenic including some pebbles (Piper and Panagos, 1979 and Table 4). This observation on the grain-size repartition is in line with the observations on the currents, with faster high-tide bottom currents swiping the middle terrace and slower low-tide surface currents affecting the shallower terrace. This grain-size repartition further support that the currents flow with their maximum velocity near the strait axis whereas the currents are depleted in energy towards the margins as suggested from ancient and modern examples by Longhitano and Chiarella (2020).

The Rion strait-center plateau has been drilled for the bridge construction and the drilling report indicate a poorly consolidated and heterolytic formation with a high grain size variability from clay to gravels (Yang et al., 2001) interpreted as an unconsolidated fluviatile formation accumulated before the Holocene. On its surface, the plateau is covered by rock-paved surface encrusted by living red corals and sponges (Table 4). These shallow-water bioherms are usually found in areas with strong bottom currents (Grigg, 1984). This surface constitutes a hardground which protects the underlying unconsolidated sediments (Yang et al., 2001).

Along the axis defined by the deepest parts of the Nafpaktos and Mornos areas, we observe large scale scouring, cross-stratifications and sediment veneering with wave length of km long and amplitude of tens of meters deep (Figs. 8B, 10B, 13). In the Nafpaktos bay, the large gutter is made of bioclastic gravels and silts (Beckers et al., 2016).

The slopes of the Nafpaktos and Mornos zones are steeper in the South than in the North, at the exception of the eastern tip of the Mornos area. The surficial sediment distribution mapped by Piper et al. (1980) showed that the steeper southern slopes are made of coarse-grained sand and gravels, and the gentle northern slopes consists of fine-grained silt and clay (Table 4). The uplift of the southern coast increases the Drepano river slope and thus the sediment supply and the grain size of its delta in comparison with the subsiding northern as also reported in the Corinth Gulf by Poulos et al. (1996). Moreover, it is also possible that the bottom currents are faster along the southern shore than along the northern shore (Beckers et al., 2016).

5.2. Expression of the internal tide on the strait seafloor

The Rion Strait shows a large diversity of depositional and erosional

Table 4

Morphologies associated with grain size from Piper and Panagos (1979) and Piper et al. (1980); current pattern and interpretations along the strait profile.

| Strait zone (bathymetry)		Patras sill (<50 m)	Patras zone (~80 m)	Rion strait-center zone (~65 m)	Nafpaktos zone (~110 m)	Mornos zone (>110 m)
Morphologies (grain size)	Northern slope	Gentle slope (Mud)	Normal faults Terraces: - Shallow (silty sand) - Deep (sand)	Cliffs (?)	Plastered drift (Mud, Silt)	Gilbert-type delta Drift (Mud, Silt)
	Strait-center	Sediment barrier (Mud and gravelly mud)	Pools and crests (Gravely sand with pebbles)	Plateau Moat; Mount; Pools (Conglomerates rock-paved surface encrusted by corals)	Pool Gutter (Gravely sand with pebbles?)	Large chutes-and-pools Canyon head (?)
	Southern slope	Gentle slope (Mud)	Delta Terrace Steep slope (?)	Cliffs (?)	Plastered slope (sandy silt)	Spit Gilbert-type delta (?)
Current pattern		Eddies on the western side of the Patras sill	Dominated by tidal currents (slopes) and high-tide internal wave (axis)	Dominated by tidal currents and high-tide internal wave	Dominated by tidal currents (slopes) and low-tide internal wave (axis)	Internal tide bottom currents
Interpretations		Depositional area at the frontier between the Patras eddies and the strait amplified tidal currents	Bypass on the slopes with abrasion terraces Erosion by bottom currents, probably carrying granules to pebbles to erode the poll and to form the crest morphologies	Bypass on the plateau (axis) and erosion in the pools and the moat by dense bottom currents: the high-tide internal waves	Erosion on the axis (pools) and deposition on the slopes (plastered drift and slope)	The spit is located at the frontier between internal wave upwelling currents and tidal currents. Erosion and deposition on the axis by supercritical to critical bottom currents (chutes-and-pools) The northern slope (eastern Mornos delta) is reworked by upwelling from Corinth Gulf
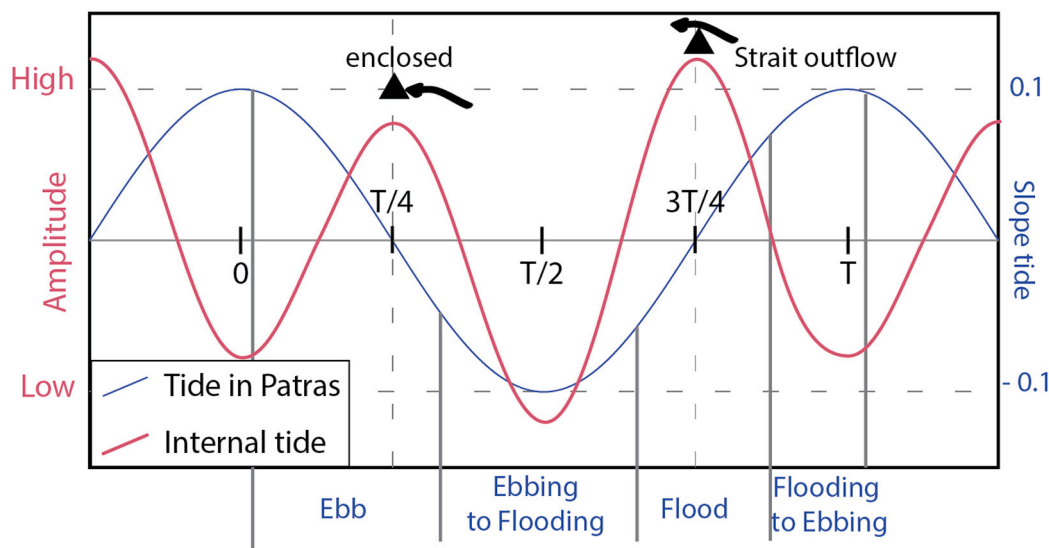
Fig. 14. Amplitude of tide and internal tide during time. The tide reference is located in the Patras Gulf.

features (Table 4). These features are shaped by an asymmetric hydro-sedimentary system dominated by tides and internal tides. The Rion Strait presents some differences with the depositional model for tidal straits proposed by Longhitano (2013).

Indeed, the lack of dunes and more generally the lack of tidal deposits is problematic. Instead of the dune-bedded strait zone with 3D and 2D tidal dunes, we observe deep pools with steep borders, interpreted as erosional areas with coarse-grained sediments, pebbles and sand carried by turbulent bottom currents, which digs the seafloor by analogy with the stream pothole (Figs. 11, 12). Another example of pools and crests has been observed in the Strait of Gibraltar in the bathymetry provided by Luján et al. (2011). Similarly, the morphologies on each side of the Carminal sill (i.e. in the Levante Basin, south of Mesata, and in the

Poniente Basin) display a rough relief formed by circular to elongated depressions limited by crests called scarps and crests by Luján et al. (2011). Plomino et al. (unpublished data) proposed that these oval-shaped scarps in the Levante basin result from bottom current induced erosion. The present study raises the possibility that the usual dune-bedded strait zones can be dominated by pool-and-crest morphology in relation with seafloor erosion on each sides of the sill by the internal tides. We suppose that turbulent flowing play a key role in this case. As modelled for Gibraltar, the tidal water stratified exchanges are very complex in the strait and generates at the sills internal hydraulic jumps and active turbulent patches which reach the seafloor (Hilt et al., 2020). Moreover, Droghei et al. (2016) have documented another example of the interaction between Internal Solitary Waves (ISWs) and the

sediment resuspension in the Messina Strait. They reported that a deep sand-wave field is due to the refraction of ISWs (induced by tide) which induce a unidirectional momentum to a fluid parcel. However, the findings of the current study have documented bidirectional bottom currents which differ from the ISW unidirectional currents.

In the Nafpaktos and Mornos bays, our results are in agreement with the previous work of Beckers et al. (2016). They suggested a water circulation with two water layers, with the exception of the summer with three water layers. They also proposed that the scours are the result of turbulent flow or lee waves based on seismic architectures and CTD. We complete this reconstruction with the evidence of an internal tide in the Corinth Gulf that is much more energetic than the tidal strait currents and explain the presence of strong bottom currents in the deeper Nafpaktos bay. As reported by Beckers et al. (2016), the plastered and slope drifts of the Nafpaktos bay are quite similar to the plastered drifts in the Alboran Sea, east of the Strait of Gibraltar where the water masses are also well contrasted (Ercilla et al., 2015). We can suggest that the plastered and slope drifts could be considered as new elements of the strait-margin zone of the tidal strait model (sensu Longhitano and Chiarella, 2020).

6. Conclusions

The aim of the present research was to examine the Rion Strait morpho-bathymetry and current dynamics to unravel the hydro-sedimentary processes in a micro-tidal environment. This study identified three sills between the shallow Patras and the deep Corinth Gulfs: 1) a sedimentary ridge in the Patras area (~50 m), the Rion Strait sill (68.7 m) and the Nafpaktos-Mornos sill (98 m). The current analyses in the strait shown a robust correlation between the flow direction and the tides, with tidal currents amplified up to 1 m/s. Despite the flow currents documented in this tidal strait system, the morpho-bathymetry revealed a sedimentary system lacking of dune fields on each side of the strait in contrast to what is expected in tidal straits (Longhitano and Chiarella, 2020). The Rion Strait is in fact dominated by erosional, rather than depositional, features. We documented a pool-and-crest erosive morphology which consists of oval bathymetric depressions of ~10 m deep and ~100 m in diameter limited by vertical crests.

This research also evidenced the occurrence of an internal tide from the Corinth Gulf. The internal tide generates high velocity bottom currents and upwellings in the Mornos and Nafpaktos bays. The velocity of these bottom currents is faster than tidal flow funneled by the strait. The findings of this study suggested that the interaction of the tides and the internal tide at the constriction point of the Rion Strait generated lee waves and turbulent erosions on each side of the strait plateau, which dig the observed pool-and-crest morphologies. On the strait margins, the sediments are veneered on the slope and formed plastered and slope drifts. A possible implication of this work is that the pool-and-crest and the drift morphologies in the straits are associated with internal tides and more generally internal waves. The major limitation of this study is the short period of data acquisition which cannot reflect all the tidal, meteorological, seasonal and interannual variations. Despite these limitations, the study certainly improves our understanding of tidal strait depositional models and processes by providing a case study dominated by an internal tide. Further studies need to be carried out based on continuous long-term current meter measurements in order to fully understand the complexity of the flow pattern.

Supplementary data to this article can be found online at https://doi.org/10.1016/j.margeo.2022.106771

Research data statement

Multibeam bathymetry is available as Geotiff on the open scientific repository www.pangaea.de with the reference: Christodoulou, Dimitris; Fakiris, Elias; Dimas, Xenophon; Rubi, Romain; Hubert-Ferrari, Aurélia; Geraga, Maria; Papatheodorou, George (2021): Multibeam bathymetry processed data (SeaBeam 1158 entire dataset) surveyed in 2019 at the Rion–Antirion Bridge, eastern Gulf of Patras and western Gulf of Corinth. PANGAEA, doi:https://doi.org/10.1594/PANGAEA.938342

The other data are available upon the request to the corresponding author: romain.rubi@uliege.be

References

Alford, M.H., MacKinnon, J.A., Nash, J.D., Simmons, H., Pickering, A., Klymak, J.M., Pinkel, R., Sun, O., Rainville, L., Musgrave, R., et al., 2011. Energy flux and dissipation in Luzon Strait: two tales of two ridges. J. Phys. Oceanogr. 41, 2211–2222.

Alpers, W., Brandt, P., Rubino, A., Backhaus, J.O., 1996. Recent contributions of remote sensing to the study of internal waves in the straits of Gibraltar and Messina. Bull. Inst. Oceanogr. Monaco-Num. Spec. 21–40.

Anderson, J.J., Carmack, E.C., 1973. Some physical and chemical properties of the Gulf of Corinth. Estuar. Coast. Mar. Sci. 1, 195–202.

Androsov, A., Voltzinger, N., Kagan, B., Salusti, E., 1993. Residual tidal circulation in the Strait of Messina. Izvestiâ Akademii nauk SSSR. Fizika atmosfery i okeana 29, 543–552.

Armijo, R., Meyer, B., King, G., Rigo, A., Papanastassiou, D., 1996. Quaternary evolution of the Corinth Rift and its implications for the Late Cenozoic evolution of the Aegean. Geophys. J. Int. 126, 11–53.

Avallone, A., Briole, P., Agatza-Balodimou, A.M., Billiris, H., Charade, O., Mitsakaki, C., Nercessian, A., Papazissi, K., Paradissis, D., Veis, G., 2004. Analysis of eleven years of deformation measured by GPS in the Corinth Rift Laboratory area. Compt. Rendus Geosci. 336, 301–311.

Beckers, A., Hubert-Ferrari, A., Beck, C., Bodeux, S., Tripsanas, E., Sakellariou, D., De Batist, M., 2015. Active faulting at the western tip of the Gulf of Corinth, Greece, from high-resolution seismic data. Mar. Geol. 360, 55–69. https://doi.org/10.1016/j.margeo.2014.12.003.

Beckers, A., Beck, C., Hubert-Ferrari, A., Tripsanas, E., Crouzet, C., Sakellariou, D., Papatheodorou, G., De Batist, M., 2016. Influence of bottom currents on the sedimentary processes at the western tip of the Gulf of Corinth, Greece. Mar. Geol. 378, 312–332. https://doi.org/10.1016/j.margeo.2016.03.001.

Bell, R.E., McNeill, L.C., Bull, J.M., Henstock, T.J., 2008. Evolution of the offshore western Gulf of Corinth. Geol. Soc. Am. Bull. 120, 156–178.

Bell, R.E., McNeill, L.C., Henstock, T.J., Bull, J.M., 2011. Comparing extension on multiple time and depth scales in the Corinth Rift, Central Greece: extension across the Corinth Rift. Geophys. J. Int. 186, 463–470. https://doi.org/10.1111/j.1365-246X.2011.05077.x.

Bignami, F., Salusti, E., Schiarini, S., 1990. Observations on a bottom vein of dense water in the Southern Adriatic and Ionian Seas. J. Geophys. Res. Oceans 95, 7249–7259.

Bleistein, N., Cohen, J.K., Stockwell Jr., J.W., Berryman, J., 2001. Mathematics of multidimensional seismic imaging, migration, and inversion. Interdisciplinary applied mathematics, Vol 13. Appl. Mech. Rev. 54, B94–B96.

Boyce, F., 1975. Internal waves in the Straits of Gibraltar. In: Deep Sea Research and Oceanographic Abstracts. Elsevier, pp. 597–610.

Brandt, P., Rubino, A., Alpers, W., Backhaus, J.O., 1997. Internal waves in the Strait of Messina studied by a numerical model and synthetic aperture radar images from the ERS 1/2 satellites. J. Phys. Oceanogr. 27, 648–663.

Briole, P., Rigo, A., Lyon-Caen, H., Ruegg, J.C., Papazissi, K., Mitsakaki, C., Balodimou, A., Veis, G., Hatzfeld, D., Deschamps, A., 2000. Active deformation of the Corinth rift, Greece: results from repeated Global Positioning System surveys between 1990 and 1995. J. Geophys. Res. 105, 25605.

Buijsman, M., McWilliams, J., Jackson, C., 2010. East-west asymmetry in nonlinear internal waves from Luzon Strait. J. Geophys. Res. Oceans 115.

Candela, J., Winant, C.D., Bryden, H.L., 1989. Meteorologically forced subinertial flows through the Strait of Gibraltar. J. Geophys. Res. Oceans 94, 12667–12679.

Cartigny, M.J.B., Ventra, D., Postma, G., van Den Berg, J.H., 2014. Morphodynamics and sedimentary structures of bedforms under supercritical-flow conditions: new insights

from flume experiments. Sedimentology 61, 712–748. https://doi.org/10.1111/sed.12076.

Chao, S.-Y., Ko, D.-S., Lien, R.-C., Shaw, P.-T., 2007. Assessing the west ridge of Luzon Strait as an internal wave mediator. J. Oceanogr. 63, 897–911.

Defant, A., 1961. Physical oceanography. Pergamon.

Droghei, R., Falcini, F., Casalbore, D., Martorelli, E., Mosetti, R., Sannino, G., Santoleri, R., Chiocci, F., 2016. The role of internal solitary waves on deep-water sedimentary processes: the case of up-slope migrating sediment waves off the Messina Strait. Sci. Rep. 6, 1–8.

Ercilla, G., Juan, C., Alonso, B., Estrada, F., Vázquez, J., Casas, D., Hernández-Molina, F. J., El Moumni, B., D'Acremont, E., Gorini, C., 2015. Interaction between Alongslope and Downslope Sedimentary Processes in the Alboran Sea during the Pliocene and Quaternary.

Evans, P., Mason-Jones, A., Wilson, C., Wooldridge, C., O'Doherty, T., O'Doherty, D., 2015. Constraints on extractable power from energetic tidal straits. Renew. Energy 81, 707–722.

Fakiris, E., Blondel, P., Papatheodorou, G., Christodoulou, D., Dimas, X., Georgiou, N., Kordella, S., Dimitriadis, C., Rzhanov, Y., Geraga, M., et al., 2019. Multi-frequency, multi-sonar mapping of shallow habitats—Efficacy and management implications in the national marine park of Zakynthos, Greece. Remote Sens. 11, 461.

Farmer, D.M., Alford, M.H., Lien, R.-C., Yang, Y.J., Chang, M.-H., Li, Q., 2011. From Luzon Strait to Dongsha Plateau: stages in the life of an internal wave. Oceanography 24, 64–77.

Ferentinos, G., Brooks, M., Doutsos, T., 1985. Quaternary tectonics in the Gulf of Patras, western Greece. J. Struct. Geol. 7, 713–717. https://doi.org/10.1016/0191-8141(85)90146-4.

Ferranti, L., Monaco, C., Morelli, D., Tonielli, R., Tortorici, L., Badalini, M., 2008. Morphostructural setting and active faults in the Messina Strait: new evidence from marine geological data. Rend. Online Soc. Geol. Ital. 1, 86–88.

Ford, M., Rohais, S., Williams, E.A., Bourlange, S., Jousselin, D., Backert, N., Malartre, F., 2013. Tectono-sedimentary evolution of the western Corinth rift (Central Greece). Basin Res. 25, 3–25.

Fourniotis, N.Th., Horsch, G.M., 2010. Three-dimensional numerical simulation of wind-induced barotropic circulation in the Gulf of Patras. Ocean Eng. 37, 355–364. https://doi.org/10.1016/j.oceaneng.2010.01.002.

Fourniotis, N.T., Horsch, G.M., 2015. Baroclinic circulation in the Gulf of Patras (Greece). Ocean Eng. 104, 238–248.

Friligos, N., Theocharis, A., Georgopoulos, D., 1985. Preliminary chemical and physical observations during summer 1980 on a silled embayment in the Ionian Sea. Vie et Milieu/Life Environ. 115–125.

García Lafuente, J., Sánchez Román, A., Díaz del Río, G., Sannino, G., Sánchez Garrido, J., 2007. Recent observations of seasonal variability of the Mediterranean outflow in the Strait of Gibraltar. J. Geophys. Res. Oceans 112.

Gibbard, P., 1995. The formation of the Strait of Dover. Geol. Soc. Lond., Spec. Publ. 96, 15–26.

Griffa, A., Marullo, S., Santoleri, R., Viola, A., 1986. Internal nonlinear tidal waves generated at the Strait of Messina. Cont. Shelf Res. 6, 677–687.

Grigg, R.W., 1984. Resource management of precious corals: a review and application to shallow water reef building corals. Mar. Ecol. 5 (1), 57–74.

Gupta, S., Collier, J.S., Garcia-Moreno, D., Oggioni, F., Trentesaux, A., Vanneste, K., De Batist, M., Camelbeeck, T., Potter, G., Van Vliet-Lanoë, B., Arthur, J.C.R., 2017. Two-stage opening of the Dover Strait and the origin of island Britain. Nat. Commun. 8, 15101. https://doi.org/10.1038/ncomms15101.

Haddad, A., Ganas, A., Kassaras, I., Lupi, M., 2020. Seismicity and geodynamics of western Peloponnese and central Ionian Islands: insights from a local seismic deployment. Tectonophysics 778, 228353. https://doi.org/10.1016/j.tecto.2020.228353.

Hadjitheodorou, C., Antonopoulos, J., Lascaratos, A., Papageorgiou, E., Trova, E., 1992. Investigation of the sea currents in the area of Rio-Antirio for the bridging project. Final Report. University of Patras Department of Civil Engineering, Patras, Greece, 296 p. (in Greek).

Hageman, J., 1979. Benthic Foraminiferal Assemblages from Plio-Pleistocene Open bay to Lagoonal Sediments of the Western Peloponnesus (Greece) (PhD Thesis). Utrecht University.

Haslinger, F., 1998. Velocity Structure, Seismicity and Seismotectonics of Northwestern Greece between the Gulf of Arta and Zakynthos (PhD Thesis). ETH Zurich.

Hatzfeld, D., Kassaras, I., Panagiotopoulos, D., Amorese, D., Makropoulos, K., Karakaisis, G., Coutant, O., 1995. Microseimicity and strain pattern in northwestern Greece. Tectonics 14, 773–785.

Hergarten, S., Robl, J., Stüwe, K., 2014. Extracting topographic swath profiles across curved geomorphic features. Earth Surf. Dynam. 2, 97–104.

Hibiya, T., 1990. Generation mechanism of internal waves by a vertically sheared tidal flow over a sill. J. Geophys. Res. Oceans 95, 1757–1764.

Hilt, M., Auclair, F., Benshila, R., Bordois, L., Capet, X., Debreu, L., Dumas, F., Jullien, S., Lemarié, F., Marchesiello, P., et al., 2020. Numerical modelling of hydraulic control, solitary waves and primary instabilities in the Strait of Gibraltar. Ocean Model 151, 101642.

Holloway, P.E., 1987. Internal hydraulic jumps and solitons at a shelf break region on the Australian North West Shelf. J. Geophys. Res. 92, 5405. https://doi.org/10.1029/JC092iC05p05405.

Horsch, G.M., Fourniotis, N.Th., 2017. Wintertime Tidal Hydrodynamics in the Gulf of Patras, Greece. J. Coast. Res. 336, 1305–1314. https://doi.org/10.2112/JCOASTRES-D-16-00133.1.

Horsch, G., Fourniotis, N., 2018. On strong nearshore wind-induced currents in flow-through Gulfs: variations on a theme by Csanady. Water 10, 652. https://doi.org/10.3390/w10050652.

Huang, X., Zhao, W., Tian, J., Yang, Q., 2014. Mooring observations of internal solitary waves in the deep basin west of Luzon Strait. Acta Oceanol. Sin. 33, 82–89.

Jackson, J.A., Gagnepain, J., Houseman, G., King, G.C.P., Papadimitriou, P., Soufleris, C., Virieux, J., 1982. Seismicity, normal faulting, and the geomorphological development of the Gulf of Corinth (Greece): the Corinth earthquakes of February and March 1981. Earth Planet. Sci. Lett. 57, 377–397.

Jan, S., Lien, R.-C., Ting, C.-H., 2008. Numerical study of baroclinic tides in Luzon Strait. J. Oceanogr. 64, 789–802. https://doi.org/10.1007/s10872-008-0066-5.

Kassaras, I., Kapetanidis, V., Karakonstantis, A., Kaviris, G., Papadimitriou, P., Voulgaris, N., Makropoulos, K., Popandopoulos, G., Moshou, A., 2014. The April–June 2007 Trichonis Lake earthquake swarm (W. Greece): New implications toward the causative fault zone. J. Geodyn. 73, 60–80.

Krijgsman, W., Hilgen, F.J., Raffi, I., Sierro, F., Wilson, D., 1999. Chronology, causes and progression of the Messinian salinity crisis. Nature 400, 652–655.

Krijgsman, W., Capella, W., Simon, D., Hilgen, F.J., Kouwenhoven, T.J., Meijer, P.T., Sierro, F.J., Tulbure, M.A., van den Berg, B.C., van der Schee, M., et al., 2018. The Gibraltar corridor: watergate of the Messinian salinity crisis. Mar. Geol. 403, 238–246.

La Violette, P.E., Arnone, R.A., 1988. A tide-generated internal waveform in the western approaches to the Strait of Gibraltar. J. Geophys. Res. 93, 15653.

Lascaratos, A., Salusti, E., Papageorgaki, G., 1989. Wind-induced upwellings and currents in the gulfs of Patras, Nafpaktos and Korinthos, Western Greece. Oceanol. Acta 12, 159–164.

Legg, S., Klymak, J., 2008. Internal hydraulic jumps and overturning generated by tidal flow over a tall steep ridge. J. Phys. Oceanogr. 38, 1949–1964. https://doi.org/10.1175/2008JPO3777.1.

Liao, G., Yuan, Y., Yang, C., Chen, H., Wang, H., Huang, W., 2012. Current observations of internal tides and parametric subharmonic instability in Luzon Strait. Atmosphere-Ocean 50, 59–76.

Lindstrom, E., Butt, J., Lukas, R., Godfrey, S., 1990. The flow through Vitiaz Strait and St. George's Channel, Papua New Guinea. In: Pratt, L.J. (Ed.), The Physical Oceanography of Sea Straits. Springer Netherlands, Dordrecht, pp. 171–189. https://doi.org/10.1007/978-94-009-0677-8_7.

Longhitano, S.G., 2013. A facies-based depositional model for ancient and modern, tectonically-confined tidal straits. Terra Nova 25, 446–452. https://doi.org/10.1111/ter.12055.

Longhitano, S.G., 2018a. Between Scylla and Charybdis (part 1): the sedimentary dynamics of the modern Messina Strait (central Mediterranean) as analogue to interpret the past. Earth Sci. Rev. 185, 259–287. https://doi.org/10.1016/j.earscirev.2018.06.008.

Longhitano, S.G., 2018b. Between Scylla and Charybdis (part 2): the sedimentary dynamics of the ancient, Early Pleistocene Messina Strait (central Mediterranean) based on its modern analogue. Earth Sci. Rev. 179, 248–286. https://doi.org/10.1016/j.earscirev.2018.01.017.

Longhitano, S.G., Chiarella, D., 2020. Chapter 15 - Tidal straits: basic criteria for recognizing ancient systems from the rock record. In: Scarselli, N., Adam, J., Chiarella, D., Roberts, D.G., Bally, A.W. (Eds.), Regional Geology and Tectonics (Second Edition). Elsevier, pp. 365–415. https://doi.org/10.1016/B978-0-444-64134-2.00014-6.

Longhitano, S.G., Chiarella, D., Muto, F., 2014. Three-dimensional to two-dimensional cross-strata transition in the lower Pleistocene Catanzaro tidal strait transgressive succession (southern Italy). Sedimentology 61, 2136–2171. https://doi.org/10.1111/sed.12138.

Luján, M., Crespo-Blanc, A., Comas, M., 2011. Morphology and structure of the Camarinal Sill from high-resolution bathymetry: evidence of fault zones in the Gibraltar Strait. Geo-Mar. Lett. 31, 163–174. https://doi.org/10.1007/s00367-010-0222-y.

Lykousis, V., Sakellariou, D., Moretti, I., Kaberi, H., 2007. Late Quaternary basin evolution of the Gulf of Corinth: sequence stratigraphy, sedimentation, fault–slip and subsidence rates. Tectonophysics 440, 29–51. https://doi.org/10.1016/j.tecto.2006.11.007.

Malikides, M., Harris, P., Jenkins, C., Keene, J., 1988. Carbonate sandwaves in Bass Strait. Aust. J. Earth Sci. 35, 303–311.

McNeill, L.C., Shillington, D.J., Carter, G.D.O., Everest, J.D., Gawthorpe, R.L., Miller, C., Phillips, M.P., Collier, R.E.Ll, Cvetkoska, A., De Gelder, G., Diz, P., Doan, M.-L., Ford, M., Geraga, M., Gillespie, J., Hemelsdaël, R., Herrero-Bervera, E., Ismaiel, M., Janikian, L., Kouli, K., Le Ber, E., Li, S., Maffione, M., Mahoney, C., Machlus, M.L., Michas, G., Nixon, C.W., Oflaz, S.A., Omale, A.P., Panagiotopoulos, K., Pechlivanidou, S., Sauer, S., Seguin, J., Sergiou, S., Zakharova, N.V., Green, S., 2019. High-resolution record reveals climate-driven environmental and sedimentary changes in an active rift. Sci. Rep. 9, 3116. https://doi.org/10.1038/s41598-019-40022-w.

Menant, A., Jolivet, L., Vrielynck, B., 2016. Kinematic reconstructions and magmatic evolution illuminating crustal and mantle dynamics of the eastern Mediterranean region since the late Cretaceous. Tectonophysics 675, 103–140.

Moretti, I., Sakellariou, D., Lykousis, V., Micarelli, L., 2003. The Gulf of Corinth: an active half graben? J. Geodyn. 36, 323–340.

Moretti, I., Lykousis, V., Sakellariou, D., Reynaud, J.-Y.Y., Benziane, B., Prinzhoffer, A., 2004. Sedimentation and subsidence rate in the Gulf of Corinth: what we learn from the Marion Dufresne's long-piston coring. Compt. Rendus Geosci. 336, 291–299.

Morozov, E.G., Trulsen, K., Velarde, M.G., Vlasenko, V.I., 2002. Internal Tides in the Strait of Gibraltar. J. Phys. Oceanogr. 32, 14.

Morozov, E.G., Parrilla-Barrera, G., Velarde, M.G., Scherbinin, A.D., 2003. The straits of Gibraltar and Kara Gates: a comparison of internal tides. Oceanol. Acta 26, 231–241. https://doi.org/10.1016/S0399-1784(03)00023-9.

Morozov, E.G., Paka, V.T., Bakhanov, V.V., 2008. Strong internal tides in the Kara Gates Strait. Geophys. Res. Lett. 35, L16603. https://doi.org/10.1029/2008GL033804.

Morozov, E.G., Kozlov, I.E., Shchuka, S.A., Frey, D.I., 2017. Internal tide in the Kara Gates Strait. Oceanology 57, 8–18. https://doi.org/10.1134/S0001437017010106.

Nixon, C.W., McNeill, L.C., Bull, J.M., Bell, R.E., Gawthorpe, R.L., Henstock, T.J., Christodoulou, D., Ford, M., Taylor, B., Sakellariou, D., Ferentinos, G., Papatheodorou, G., Leeder, M.R., Collier, R.E.L.I., Goodliffe, A.M., Sachpazi, M., Kranis, H., 2016. Rapid spatiotemporal variations in rift structure during development of the Corinth Rift, central Greece: rapid changes in rift structure, Corinth. Tectonics 35, 1225–1248. https://doi.org/10.1002/2015TC004026.

Papadopoulos, G.A., Karastathis, V.K., Koukouvelas, I., Sachpazi, M., Baskoutas, I., Chouliaras, G., Agalos, A., Daskalaki, E., Minadakis, G., Moshou, A., 2014. The Cephalonia Ionian Sea (Greece), sequence of strong earthquakes of January–February 2014: a first report. Res. Geophys 4.

Papailiou, D., 1982. Oceanographical study in Patras Gulf waters for pollution management, II. University of Patras, Dept. of Mechanical Engineering, Patras, Greece (in Greek).

Papanikolaou, D.J., Royden, L.H., 2007. Disruption of the Hellenic arc: Late Miocene extensional detachment faults and steep Pliocene-Quaternary normal faults - Or what happened at Corinth? Tectonics 26, 1–16.

Papatheodorou, G., Geraga, M., Christodoulou, D., Iatrou, M., Fakiris, E., Heath, S., Baika, K., 2014. A marine geoarchaeological survey, cape Sounion, Greece: preliminary results. Mediter. Archaeol. Archaeom. 14, 357–371.

Perissoratis, C., Piper, D.J.W., Lykousis, V., 2000. Alternating marine and lacustrine sedimentation during late Quaternary in the Gulf of Corinth rift basin, central Greece. Mar. Geol. 167, 391–411. https://doi.org/10.1016/S0025-3227(00)00038-4.

Pérouse, E., Sébrier, M., Braucher, R., Chamot-Rooke, N., Bourlès, D., Briole, P., Sorel, D., Dimitrov, D., Arsenikos, S., 2017. Transition from collision to subduction in Western Greece: the Katouna–Stamna active fault system and regional kinematics. Int. J. Earth Sci. (Geol. Rundsch) 106, 967–989. https://doi.org/10.1007/s00531-016-1345-9.

Pinkel, R., Buijsman, M., Klymak, J.M., 2012. Breaking topographic lee waves in a tidal channel in Luzon Strait. Oceanography 25, 160–165.

Piper, D., Panagos, A., 1979. Marine geology of the Gulf of Patras. Thalassographica 3, 5–20.

Piper, D.J.W., Kontopoulos, N., Panagos, A., 1980. Deltaic, coastal and shallow marine sediments of the western gulf of Corinth. Thalassographica 2, 5–14.

Piper, D.J.W., Kontopoulos, N., Panagos, A.G., 1988. Deltaic sedimentation and stratigraphic sequences in post-orogenic basins, Western Greece. Sediment. Geol. 55, 283–294. https://doi.org/10.1016/0037-0738(88)90135-2.

Pistek, P., La Violette, P.E., 1999. Observations of the suppression of tide-generated nonlinear internal wave packets in the Strait of Gibraltar. J. Mar. Syst. 20, 113–128. https://doi.org/10.1016/S0924-7963(98)00073-6.

Poulos, S.E., Collins, M.B., Pattiaratchi, C., Cramp, A., Gull, W., Tsimplis, M., Papatheodorou, G., 1996. Oceanography and sedimentation in the semi-enclosed, deep-water Gulf of Corinth (Greece). Mar. Geol. 134, 213–235.

Pratt, L., Lundberg, P., 1991. Hydraulics of rotating strait and sill flow. Annu. Rev. Fluid Mech. 23, 81–106.

Pugh, D.T., 1987. Tides, Surges and Mean Sea Level.

Rainville, L., Lee, C.M., Rudnick, D.L., Yang, K.-C., 2013. Propagation of internal tides generated near Luzon Strait: observations from autonomous gliders. J. Geophys. Res. Oceans 118, 4125–4138.

Reynaud, J.-Y., Ferrandini, M., Ferrandini, J., Santiano, M., Thinon, I., André, J.-P., Barthet, Y., Guennoc, P., Tessier, B., 2013. From non-tidal shelf to tide-dominated strait: the Miocene Bonifacio Basin, Southern Corsica. Sedimentology 60, 599–623. https://doi.org/10.1111/j.1365-3091.2012.01352.x.

Rudnick, D.L., Johnston, T.S., Sherman, J.T., 2013. High-frequency internal waves near the Luzon Strait observed by underwater gliders. J. Geophys. Res. Oceans 118, 774–784.

Sachpazi, M., Hirn, A., Clément, C., Haslinger, F., Laigle, M., Kissling, E., Charvis, P., Hello, Y., Lépine, J.-C., Sapin, M., et al., 2000. Western Hellenic subduction and Cephalonia Transform: local earthquakes and plate transport and strain. Tectonophysics 319, 301–319.

Sachpazi, M., Clément, C., Laigle, M., Hirn, A., Roussos, N., Clément, C., Laigle, M., Hirn, A., Roussos, N., 2003. Rift structure, evolution, and earthquakes in the Gulf of Corinth, from reflection seismic images. Earth Planet. Sci. Lett. 216, 243–257.

Sakellariou, D., Lykousis, V., Papanikolaou, D., 2001. Active faulting in the Gulf of Corinth, Greece. In: 36th CIESM Congress Proceedings, pp. 36–43.

Sánchez-Garrido, J.C., Sannino, G., Liberti, L., García Lafuente, J., Pratt, L., 2011. Numerical modeling of three-dimensional stratified tidal flow over Camarinal Sill, Strait of Gibraltar. J. Geophys. Res. 116, C12026.

Santoro, V.C., Amore, E., Cavallaro, L., Cozzo, G., Foti, E., 2002. Sand waves in the Messina strait, Italy. J. Coast. Res. 640–653.

Sapia, A., Salusti, E., 1987. Observation of nonlinear internal solitary wave trains at the northern and southern mouths of the Strait of Messina. Deep Sea Res. Part A Oceanogr. Res. Pap. 34, 1081–1092.

Schlitzer, R., 2015. Ocean Data View.

Shanmugam, G., Wang, Y., 2014. Review of research in internal-wave and internal-tide deposits of China: discussion. J. Palaeogeogr. 3 (4), 332–350. ISSN 2095-3836.

Shepard, F.P., 1975. Progress of internal waves along submarine canyons. Mar. Geol. 19 (3), 131–138.

Stow, D.A.V., Hernández-Molina, F.J., Llave, E., Sayago-Gil, M., Díaz del Río, V., Branson, A., 2009. Bedform-velocity matrix: the estimation of bottom current velocity from bedform observations. Geology 37, 327–330. https://doi.org/10.1130/G25259A.1.

Stow, D., Hernández-Molina, F., Llave, E., Bruno, M., García, M., del Rio, V.D., Somoza, L., Brackenridge, R., 2013. The Cadiz Contourite Channel: Sandy contourites, bedforms and dynamic current interaction. Mar. Geol. 343, 99–114.

Taylor, B., Weiss, J.R., Goodliffe, A.M., Sachpazi, M., Laigle, M., Hirn, A., 2011. The structures, stratigraphy and evolution of the Gulf of Corinth rift, Greece: structures, stratigraphy and evolution of GoC. Geophys. J. Int. 185, 1189–1219. https://doi.org/10.1111/j.1365-246X.2011.05014.x.

Tian, J., Yang, Q., Liang, X., Xie, L., Hu, D., Wang, F., Qu, T., 2006. Observation of Luzon strait transport. Geophys. Res. Lett. 33.

Vázquez, A., Bruno, M., Izquierdo, A., Macías, D., Ruiz-Cañavate, A., 2008. Meteorologically forced subinertial flows and internal wave generation at the main sill of the Strait of Gibraltar. Deep-Sea Res. I Oceanogr. Res. Pap. 55, 1277–1283.

Warn-Varnas, A., Hawkins, J., Lamb, K., Piacsek, S., Chin-Bing, S., King, D., Burgos, G., 2010. Solitary wave generation dynamics at Luzon Strait. Ocean Model 31, 9–27.

Watson, G., Robinson, I., 1990. A study of internal wave propagation in the Strait of Gibraltar using shore-based marine radar images. J. Phys. Oceanogr. 20, 374–395.

Yang, D., Dobry, R., Peck, R.B., 2001. Foundation-Soil-Inclusion Interaction Modelling for Rion-Antirion Bridge Seismic Analysis, 11. University of Missouri–Rolla.

Yuan, Y., Zheng, Q., Dai, D., Hu, X., Qiao, F., Meng, J., 2006. Mechanism of internal waves in the Luzon Strait. J. Geophys. Res. Oceans 111.

Ziegenbein, J., 1969. Short internal waves in the Strait of Gibraltar. In: Deep Sea Research and Oceanographic Abstracts. Elsevier, pp. 479–487.